

Dynamics of a rounded laminar compressible impinging jet

J. Sierra-Ausin^{1,2†}, F. Giannetti¹ and D. Fabre²

¹Institut de Mécanique des fluides de Toulouse (IMFT), Toulouse 31400, France

²Dipartimento di Ingegneria (DIIN), Università degli Studi di Salerno, Fisciano 84084, Italy

(Received xx; revised xx; accepted xx)

We study the dynamics of a rounded subsonic impinging jet. We investigate this problem by solving the compressible linearised Navier–Stokes equations around a laminar baseflow, with a normal form issued from a weakly-nonlinear approach and by means of axisymmetric time-stepping simulations. The linear stability analysis shows the existence of a family of global modes for every Mach number, which are supported by a non-local feedback loop. In order to get an insight to the core of the instability mechanisms, we propose a non-local decomposition of the structural sensitivity and the endogeneity concepts. The use of these sensitivity maps allows us to differentiate two distinct instability mechanisms. The instability is always initiated by a shear layer instability. Nonetheless, the closure of the feedback differs. At large Mach number, the production of divergence lies inside the jet, and it is responsible for the backward propagation of the guided jet mode. On the other hand, at low Mach number, the wavemaker of the instability is along the region where the module of the linearised Lamb vector is largest. Therefore, indicating that the closure mechanism is a pressure wave issued from a vortical source. We also provide a qualitative description of the tonal and broadband noise by means of the normal form of the bifurcation. Based on a phenomenological reasoning, we also suggest a stochastic model which accounts for the low coherence of the sources of sound at low Mach number. Such a model reproduces reasonably well the sound pressure level measured from time-stepping simulations.

1. Introduction – Aim of the study

It has been established that intense acoustic tonal sound is generated by the impingement of a high subsonic or supersonic jet onto a wall. Early experimental studies carried out by many researchers, including Powell (1953, 1961), Wagner (1971), Neuwerth (1974), Preisser (1979), Ho & Nosseir (1981); Nosseir & Ho (1982) observed that the frequency varies with the distance to the solid boundary, and it is organised in stages. Furthermore, the dynamics of the jet, for instance pressure in the near-field and in the far-field, were found to peak at particular frequency for high subsonic Mach numbers and to be broadband for low Mach numbers (Nosseir & Ho 1982). The staging phenomenon led Powell (1953) to conjecture that the self-sustained mechanism was a two-stage process, which involves the vortical structures convected downstream and the acoustic waves propagating upstream from the solid boundary to the nozzle. Similar feedback loops have been also observed in supersonic impinging jets. The establishment of the feedback loop has been studied experimentally by Norum (1991) and numerically by Gojon *et al.* (2016); Bogey & Gojon (2017) for ideally expanded supersonic jets. Similarly, for underexpanded jets, there is experimental evidence of the existence of the loops by Risborg & Soria

† Email address for correspondence: javier.sierra@imft.fr

(2009); Buchmann *et al.* (2011); Mitchell *et al.* (2012) and numerical by Dauptain *et al.* (2012); Gojon & Bogey (2017a). Ho & Nosseir (1981) proposed a simplified frequency selection criterion, assuming the wave propagating upstream to be a free-stream acoustic wave propagating outside the jet. Nevertheless, later studies established that the feedback loop is closed by a guided jet wave propagating mostly inside the jet (Tam & Ahuja 1990). Tam & Ahuja (1990) proposed a theoretical model for the frequency selection. The model considers a Kelvin-Helmholtz mode with a constant frequency and guided jet waves classified by their radial and azimuthal structure with different dispersion relations. The authors conjectured that the loop is closed by the Kelvin-Helmholtz mode and the least-dispersive guided wave. Following this reasoning, they concluded that tonal noise does not exist below a cut-off Mach number because the frequency of the guided waves does not match the frequency of the Kelvin-Helmholtz mode. Particularly, the properties of the guided waves, allow us to explain the frequencies and the axisymmetric or helical nature of the acoustic tones (Gojon *et al.* 2016; Bogey & Gojon 2017; Jaunet *et al.* 2019; Varé & Bogey 2022a,b). These guided waves are involved in other resonance phenomena, for examples in screech generation mechanism, as studied by Gojon & Bogey (2017b); Edgington-Mitchell *et al.* (2018); Mancinelli *et al.* (2019); Edgington-Mitchell (2019) or in jet-plate interactions, as recently investigated by Jordan *et al.* (2018); Tam & Chandramouli (2020); Varé & Bogey (2022a). They also play a role in the generation of acoustic tones near the nozzle (Towne *et al.* 2017; Brès *et al.* 2018; Bogey 2021) and in the upstream acoustic far field of free jets (Bogey 2022).

The paper aims to rationalize previous experimental results on the sound emission from a jet impinging on a perpendicular flat surface at large subsonic Mach numbers. We have several objectives. First, we analyse the properties of the feedback loop, by means of a Helmholtz-Hodge decomposition that allows a global decomposition of the flow perturbations and a local decomposition into the underpinned waves of the baseflow, i.e., we measure the relative magnitude of the acoustic and hydrodynamic components of the global mode. It results that for a sufficiently large Reynolds number, there is always a global unstable mode. However, at low and large Mach numbers of the jet, the mechanisms responsible for the closure of the feedback mechanism are distinct. In particular, that connects with the cut-off criterion of Tam & Ahuja (1990) for the existence of tonal or broadband noise. Tam & Ahuja (1990) conjectured that below the cut-off $M_c \approx 0.6$ high acoustic sound emissions are not possible because the Strouhal of the first guided wave does not match the Strouhal of the Kelvin-Helmholtz instability. Such a conclusion has been widely used in literature to justify the existence of broadband noise emissions below the cut-off Mach number. However, we will show that the feedback mechanism responsible for high acoustic tonal emissions at high subsonic Mach numbers, also exist at low Mach numbers, even at the incompressible limit for the laminar jet, nonetheless distinct closure mechanisms cause the instability. This is shown following a three-step approach:

- (i) Determine the linear global mode associated to the feedback mechanism at every Mach number.
- (ii) Determine the nature of the feedback-loop at low and high Mach numbers. We introduce a novel decomposition of the structural sensitivity map.
- (iii) Perform a wave decomposition of the feedback global mode into Kelvin-Helmholtz and guided waves.

Such a process allows us to unveil the instability core of the feedback-loop and to analyse the physical mechanisms supporting the instability. In addition, the wave decomposition allows us to determine the local characteristics in terms of waves of the loop, e.g., the reflection coefficient at neutrality.

Furthermore, we analyse the nonlinear dynamics of the impinging jet flow configuration. Specifically, we will show that the frequencies involved in the feedback process are mostly determined by geometrical features and the velocity of propagation in the medium, i.e. Mach number and convective velocity. The eigenvalues associated to the global modes are found to form a discrete arc, with a nearly constant frequency distance $\Delta\omega$. Furthermore, performing the expansion of the flow into base flow and harmonic contributions,

$$\mathbf{q}(\mathbf{x}, t) = \mathbf{q}_0(\mathbf{x}) + \sum_{k=1}^N [A_k \mathbf{q}_{A_k} e^{i\omega_k t} + \text{c.c.}] + \dots \quad (1.1)$$

where the higher harmonics and the zeroth-harmonic modification of the meanflow have been omitted. With such an ansatz, we have carried out a normal form reduction approach (Sierra-Ausín *et al.* 2022; Sierra *et al.* 2020b) to determine the reduced-order equation that governs the dynamics of the feedback mechanism, the normal form in polar coordinates $A_k = r_k e^{i\phi_k}$ is as follows

$$\begin{aligned} \dot{r}_j &= r_j (\lambda_j + \sum_k^N \nu_{jk} r_k^2) + F_{\text{res}}(\mathbf{r}, \Psi) \\ \dot{\psi}_j &= F_{\psi_j}(\mathbf{r}, \Psi). \end{aligned} \quad (1.2)$$

The vector $\mathbf{r} = [r_1, \dots, r_{N-1}]^T$ with r_j for $j = 1, \dots, N$ is the vector of (real) amplitudes proportional to each normalized global mode that characterizes the amplitude of the limit cycle, and $\Psi = [\psi_1, \dots, \psi_N]^T$ is the vector of resonant phases, where each resonant phase is a function of an imperfect quantisation of the feedback modes $\Psi_j = \Delta\phi_j - \Delta\phi_{j-1} = (\phi_{j+1} - \phi_j) - (\phi_j - \phi_{j-1})$. Herein, we treat the case with $N = 3$, and the vector fields F_{ψ_j} and F_{res} will be specified later on for this case. In the case of a perfect equi-distribution of feedback modes ($\omega_k = k\Delta\omega$), the limit cycles would be in a perfect resonance. However, nonlinear modulations of the frequency, which could be accounted by the disparity in the amplitude of local sources of divergence of the velocity field perturbations or vortex-sound responsible for the closure of the feedback-loop.

In addition, in order to model the broadband behaviour characteristic of low Mach number flows, we propose a stochastic model which is based on a phenomenological reasoning. It accounts for the low temporal coherence of the sources of sound at low Mach number, which in turn induce a frequency mismatch in the frequency selection criterion. The model is able to capture the qualitative features of low and large Mach number flows.

The outline of the manuscript is as follows. First, the flow configuration and the numerical approach are presented in section 2. Second, in section 3 we describe some basic properties of the baseflow, and we show the main results of the linear stability study, highlighting two mechanisms of closure of the feedback-mechanism. Third, in section 4 we carry out a Helmholtz-Hodge decomposition in order to get a further insight into the hydromagnetic-acoustic feedback loop by means of a novel non-local structural sensitivity decomposition. Therein, we also perform a weakly non-parallel decomposition of the global mode into the waves supported by the baseflow with the aim of determining the reflection coefficient. Then, in section 5 we analyse the interaction between limit cycles by means of axisymmetric time-stepping simulations and the normal form. Finally, in section 6 we summarise the main findings of the study.

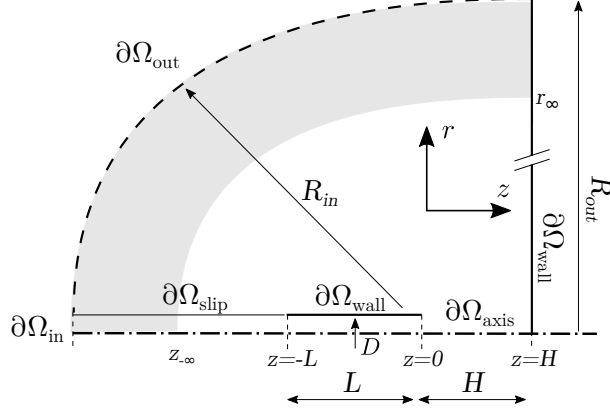


Figure 1: Diagram of the domain. The physical domain, represented as a white area, is complemented with a radial buffer layer, shown as a light grey shaded zone.

2. Numerical approach

2.1. Governing equations

Let us introduce the compressible Navier–Stokes equations as the governing equations of motion of a perfect gas described in primitive variables $\mathbf{q} = [\rho, u_r, u_\theta, u_z, p, T]^T$, and the set of control parameters $\boldsymbol{\eta} = [Re, M_\infty]^T$. These are formally expressed as

$$\mathbf{B} \frac{\partial \mathbf{q}}{\partial t} = \mathbf{F}(\mathbf{q}, \boldsymbol{\eta}) \quad \text{with } \mathbf{B} = \text{diag}(1, \rho \mathbf{I}, \rho, 0), \quad (2.1)$$

$$\mathbf{F}(\mathbf{q}, \boldsymbol{\eta}) = - \begin{pmatrix} \mathbf{u} \cdot \nabla \rho + \rho \nabla \cdot \mathbf{u} \\ \rho \mathbf{u} \cdot \nabla \mathbf{u} - \nabla p + \nabla \cdot \frac{1}{Re} \tau(\mathbf{u}) \\ (\gamma - 1) \left[\rho T \nabla \cdot \mathbf{u} - \gamma \frac{M_\infty^2}{Re} \tau(\mathbf{u}) : \mathbf{D}(\mathbf{u}) \right] - \rho \mathbf{u} \cdot \nabla T + \frac{\gamma}{Pr Re} \nabla^2 T \\ -\rho T + 1 + \gamma M_\infty^2 p \end{pmatrix}, \quad (2.2)$$

The geometric configuration used in the analysis of the acoustic radiation of a rounded impinging jet is sketched in fig. 1. It consists of a pipe that is subdivided into two zones, a first pipe with slip adiabatic walls and a second pipe of length L with no-slip adiabatic walls. The physical domain, depicted as a white region in fig. 1 is complemented with an absorbing boundary layer in the far-field, which is either a complex mapping region (Sierra *et al.* 2020a) for the linear computations of section 2.2 or a sponge region (Fani *et al.* 2018) for the nonlinear computations of section 2.3. In our formulation, the primitive variables have been made dimensionless to

$$\begin{aligned} \mathbf{x} &= \frac{\tilde{\mathbf{x}}}{D}, \quad t = \frac{\tilde{t} \tilde{u}_z|_{z=0}}{D}, \quad \rho = \frac{\tilde{\rho}}{\tilde{\rho}|_{fs}}, \quad \mathbf{u} = \frac{\tilde{\mathbf{u}}}{\tilde{u}_z|_{z=0}}, \quad T = \frac{\tilde{T}}{\tilde{T}|_{fs}}, \\ p &= \frac{\tilde{p} - \tilde{p}|_{fs}}{\tilde{\rho}|_{fs} \tilde{u}_z|_{z=0}^2}, \quad M_\infty = \frac{\tilde{u}_z|_{z=0}}{(\gamma R_g \tilde{T}|_{fs})^{1/2}}, \quad Re = \frac{\tilde{\rho}|_{fs} \tilde{u}_z|_{z=0} D}{\mu(\tilde{T}|_{fs})} \end{aligned} \quad (2.3)$$

where R_g is the ideal gas constant, $\tilde{u}_z|_{z=0}$ denote the average value of the axial velocity at the cross-section $z = 0$, and $\tilde{\rho}|_{fs}$, $\tilde{p}|_{fs}$, $\tilde{T}|_{fs}$ denote the values on the far-field or free-stream. The Navier–Stokes equations eq. (2.1) are complemented with the following

boundary conditions,

$$\begin{aligned} u_z &= 1, & u_r &= 0, & T &= (1 - \frac{\gamma-1}{2} M_\infty^2) & \text{on } \partial\Omega_{in} \\ u_z &= 0, & u_r &= 0, & \nabla T \cdot \mathbf{n} &= 0 & \text{on } \partial\Omega_{wall} \\ u_r &= 0, & \nabla T \cdot \mathbf{n} &= 0 & & & \text{on } \partial\Omega_{slip} \\ \rho &= 1, & p &= 0, & T &= 1 & \text{on } \partial\Omega_{out}. \end{aligned} \quad (2.4)$$

The inlet boundary condition models the inflow from a reservoir with a constant total temperature equal to unity. In such a way, the energy of the system is kept constant for every Mach number M_∞ . The length of the pipe is a constant of the problem that determines the height of the boundary layer, here we have chosen $L = 2.5D$. The flow in the slip region is nearly constant, thus the length of this region is not an important parameter of the problem. The location of the start of the absorbing layer is chosen to be $z_{-\infty} = r_\infty = 15D$. Finally, the distance between the nozzle end location ($z = 0$) and the impinging wall is H , which is kept constant $H = 5D$.

2.2. Linear Navier–Stokes equations

The asymptotic linear stability of a steady-state \mathbf{q}_0 is examined from the temporal evolution of an infinitesimal perturbation, i.e. by performing the following expansion $\mathbf{q} = \mathbf{q}_0 + \varepsilon(\hat{\mathbf{q}}e^{-i\omega t} + \text{c.c.})$ where $\varepsilon \ll 1$. The steady-state \mathbf{q}_0 is said to be asymptotically linearly stable if there is not an eigenvalue with a positive growth rate, in other words for every eigenvalue $\omega_i < 0$, otherwise it is said to be linearly unstable. The perturbation $\hat{\mathbf{q}}$ and its eigenvalue $i\omega$ are determined by solving the following eigenvalue problem

$$-i\omega \mathbf{B}|_{\mathbf{q}_0} \hat{\mathbf{q}} + \mathbf{DF}|_{\mathbf{q}_0}(\hat{\mathbf{q}}, \boldsymbol{\eta}) = 0, \quad (2.5)$$

The linear Navier–Stokes equations eq. (2.5) are complemented with the following homogeneous boundary conditions,

$$\begin{aligned} \hat{u}_z &= 0, & \hat{u}_r &= 0, & \hat{T} &= 0 & \text{on } \partial\Omega_{in} \\ \hat{u}_z &= 0, & \hat{u}_r &= 0, & \nabla \hat{T} \cdot \mathbf{n} &= 0 & \text{on } \partial\Omega_{wall} \\ \hat{u}_r &= 0, & \nabla \hat{T} \cdot \mathbf{n} &= 0 & & & \text{on } \partial\Omega_{slip} \\ \hat{\rho} &= 0, & \hat{p} &= 0, & \hat{T} &= 0 & \text{on } \partial\Omega_{out}. \end{aligned} \quad (2.6)$$

In the following, we will also consider the adjoint eigenmode $\hat{\mathbf{q}}^\dagger$, which is a solution of the adjoint eigenvalue problem

$$i\bar{\omega} \mathbf{B}|_{\mathbf{q}_0} \hat{\mathbf{q}}^\dagger + \mathbf{DF}^\dagger|_{\mathbf{q}_0}(\hat{\mathbf{q}}^\dagger, \boldsymbol{\eta}) = 0. \quad (2.7)$$

where $\bar{\cdot}$ is employed for the complex conjugation. The boundary conditions of the adjoint problem are the same as the direct, eq. (2.6). The adjoint modes are normalised by the B -inner product, that is $\langle \hat{\mathbf{q}}^\dagger, \hat{\mathbf{q}} \rangle_{\mathbf{B}} = 1$.

2.3. Time-stepping approach

The Navier–Stokes equations (eq. (2.1)) are evolved in time with a fully implicit time integrator. We use a third order BDF scheme to integrate in time the state variable \mathbf{q} . The semi-discrete in time equations are as follows,

$$\mathbf{B} \left[\frac{11}{6} \mathbf{q}(t_{n+1}) - 3\mathbf{q}(t_n) + \frac{3}{2} \mathbf{q}(t_{n-1}) - \frac{1}{3} \mathbf{q}(t_{n-2}) \right] = -\Delta t \mathbf{F}(\mathbf{q}(t_{n+1}), \boldsymbol{\eta}) \quad (2.8)$$

Each time-step, the nonlinear problem eq. (2.8) is solved with a Newton method,

$$\begin{aligned} \left[\frac{11}{6} \mathbf{B} + \Delta t D\mathbf{F}|_{\mathbf{q}^\ell(t_{n+1})} \right] \delta \mathbf{q} &= \mathbf{B} \left[3\mathbf{q}(t_n) - \frac{3}{2}\mathbf{q}(t_{n-1}) + \frac{1}{3}\mathbf{q}(t_{n-2}) \right] - \Delta t \mathbf{F}(\mathbf{q}^\ell(t_{n+1}), \boldsymbol{\eta}) \\ \mathbf{q}^{\ell+1}(t_{n+1}) &= \mathbf{q}^\ell(t_{n+1}) + \delta \mathbf{q}. \end{aligned} \quad (2.9)$$

The assembling of the jacobian matrix $D\mathbf{F}|_{\mathbf{q}^\ell(t_{n+1})}$ is the most expensive step, and as it is conventional, a frozen jacobian matrix is adopted all along the Newton method, that is, $D\mathbf{F}|_{\mathbf{q}^\ell(t_{n+1})} = D\mathbf{F}|_{\mathbf{q}(t_n)}$. Furthermore, provided that the time-step is not too large, the jacobian matrix is kept constant for few time-steps, as long as the number of iterations to convergence of the Newton method do not drastically grow.

2.4. Normal form reduction

In the following, we summarize the normal form reduction procedure, which is carried out to study the interaction between distinct periodic orbits resulting from global instabilities associated to the main feedback mechanism. A comprehensive explanation is left to appendix B.

Near the onset of the bifurcation, dynamics can be reduced to the normal form. The coefficients of the normal form are computed following a multiple scales expansion of the solution \mathbf{q} of eq. (2.1). The expansion considers a two scale development of the original time $t \mapsto t + \varepsilon^2 \tau$, here ε is the order of magnitude of the flow disturbances, assumed small $\varepsilon \ll 1$. Herein, we consider the small parameters ε_{M^2} and ε_ν , which are a function of the Mach number and Reynolds numbers at the far-field,

$$\varepsilon_{M^2}^2 = (M_{\infty,c}^2 - M_\infty^2) \sim \varepsilon^2 \text{ and } \varepsilon_\nu^2 = (\nu_c - \nu) = (Re_c^{-1} - Re^{-1}) \sim \varepsilon^2.$$

The technique decomposes time into a fast timescale t of the phase associated to the self-sustained instabilities and a slow timescale related to the evolution of the amplitudes $z_i(\tau)$, introduced in eq. (2.11), for $i = 1, 2, 3$. The ansatz of the expansion is as follows

$$\mathbf{q}(t, \tau) = \mathbf{q}_b + \varepsilon \mathbf{q}_{(\varepsilon)}(t, \tau) + \varepsilon^2 \mathbf{q}_{(\varepsilon^2)}(t, \tau) + \varepsilon^3 \mathbf{q}_{(\varepsilon^3)}(t, \tau) + O(\varepsilon^4) \quad (2.10)$$

In the following, we shall consider the normal form equation resulting from the interaction of three modes identified by linear stability, that is,

$$\mathbf{q}_{(\varepsilon)}(t, \tau) = \sum_{k=1}^N (z_k(\tau) \hat{\mathbf{q}}_{(z_k)}(r, z) e^{i\omega_k t} + \text{c.c.}) \quad (2.11)$$

Note that the expansion of the LHS of eq. (2.1) up to third order is as follows

$$\varepsilon \mathbf{B} \frac{\partial \mathbf{q}_{(\varepsilon)}}{\partial t} + \varepsilon^2 \mathbf{B} \frac{\partial \mathbf{q}_{(\varepsilon^2)}}{\partial t} + \varepsilon^3 \left[\mathbf{B} \frac{\partial \mathbf{q}_{(\varepsilon^3)}}{\partial t} + \mathbf{B} \frac{\partial \mathbf{q}_{(\varepsilon)}}{\partial \tau} \right] + O(\varepsilon^4), \quad (2.12)$$

and the RHS respectively,

$$\mathbf{F}(\mathbf{q}, \boldsymbol{\eta}) = \mathbf{F}_{(0)} + \varepsilon \mathbf{F}_{(\varepsilon)} + \varepsilon^2 \mathbf{F}_{(\varepsilon^2)} + \varepsilon^3 \mathbf{F}_{(\varepsilon^3)} + O(\varepsilon^4). \quad (2.13)$$

Then, the problem truncated at order three is reduced to a low-dimensional system governing the complex amplitudes $z_j(t)$. Herein we consider the case of $N = 3$, the general case is briefly discussed in appendix B.5. The normal form is as follows,

$$\begin{aligned} \dot{z}_1 &= z_1 (\lambda_1 + \nu_{11} |z_1|^2 + \nu_{12} |z_2|^2 + \nu_{13} |z_3|^2) + \chi_1 z_2^2 \bar{z}_3 \\ \dot{z}_2 &= z_2 (\lambda_2 + \nu_{21} |z_1|^2 + \nu_{22} |z_2|^2 + \nu_{23} |z_3|^2) + \chi_2 z_1 \bar{z}_2 z_3 \\ \dot{z}_3 &= z_3 (\lambda_3 + \nu_{31} |z_1|^2 + \nu_{32} |z_2|^2 + \nu_{33} |z_3|^2) + \chi_3 z_2^2 \bar{z}_1 \end{aligned} \quad (2.14)$$

where $\nu_{k\ell}, \lambda_k, \chi_k \in \mathbb{C}$ for $k, \ell = 1, 2, 3$. The real part of the linear terms, named λ_k , correspond to the growth rate of the k^{th} mode. Respectively, the imaginary part of λ_k is associated to the frequency variation of the k^{th} mode with respect to the frequency

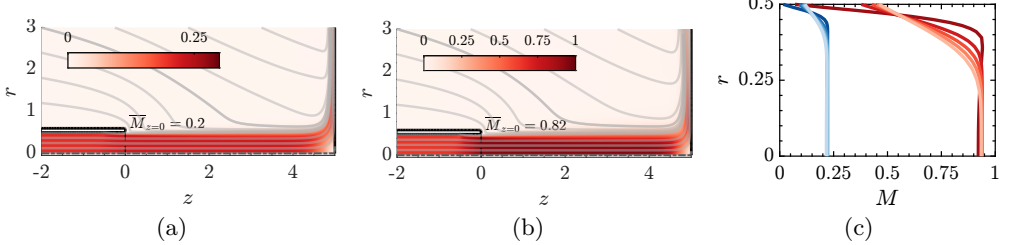


Figure 2: Spatial distribution of the Mach number for a baseflow at (a) $Re = 2200$ and $M_\infty = 0.2$, (b) $M_\infty = 0.6$ and $Re = 800$. (c) Radial evolution of the Mach number (blue for the profiles of (a) and red for (b)) from the nozzle exit ($z = 0$, represented with the darkest colour) to $z = 4D$ (light colour), with an equidistant step of a diameter.

of the neutral mode, i.e., with respect to the frequency ω_k determined from linear stability analysis. The terms $\nu_{k\ell}$ are the third order self ($k = \ell$) and cross interaction ($k \neq \ell$) coefficients. The resonant coefficients χ_k arise because of the quantization of the eigenvalues in the spectrum at a nearly constant distance $\Delta\omega$, i.e. frequency gaps $\Delta\omega_i = (\omega_{i+1} - \omega_i)$ are nearly constant, see fig. 15 (a) in appendix B.5. In the analysis, we consider that the imperfections in the frequency difference between two modes is small, that is, $(\Delta\omega_{i+1} - \Delta\omega_i) \sim \varepsilon^2$. In this way, the term $z_2^2 \bar{z}_3$ is nearly resonant with z_1 , or in other terms $\omega_2 - \Delta\omega_2 \approx \omega_1$.

3. Linear global stability procedure – Parametric analysis

3.1. Baseflow properties

We define the baseflow as the steady-state solution of the Navier–Stokes equations satisfying the boundary conditions listed in eq. (2.4). The baseflow is determined by two dimensionless parameters, the Reynolds number (Re) based on the averaged velocity at the nozzle exit and the Mach number (M_∞) based on the averaged velocity at the nozzle exit and the speed of sound at the far-field. Given this definition of the Mach number based on the speed of sound at the far field (M_∞), the actual Mach number of the flow can be considerably larger, specially for $M_\infty \in [0.5, 0.6]$, where compressibility effects are significant. Figure 2 reports the spatial distribution of the Mach number in the region between the nozzle and the impinging wall. Figure 2 (c) shows the radial evolution of the velocity profile. Since we consider a laminar baseflow the boundary layer thickness at the nozzle exit (darker velocity profile in the figure) is considerably larger than for a turbulent mean flow profile, and it is around a tenth of the diameter.

3.2. Linear stability – Compressibility effects

We analyse the effects of the Mach number on the feedback mechanism. First, we determine the dominant global linear modes for every subsonic Mach number, which corresponds to $M_\infty \in [0, 0.6]$. Figure 3 shows the neutral curves of linear stability of the steady-state. We follow the evolution of the leading five modes, which are characterised by a slow frequency evolution with respect to the Mach number and a nearly constant frequency $\Delta\omega$ distance between modes. At a given Mach number, the modes are characterised by their axial wavenumber; the dominant modes at $M_\infty = 0.6$, displayed in fig. 3 (g-i), are characterised by seven, six and eight half-wavelengths, respectively. Nonetheless, such a characterisation is not constant with varying Mach number, the number of axial wavelengths can vary up to a unit. The change of the axial wavenumber is a continuous

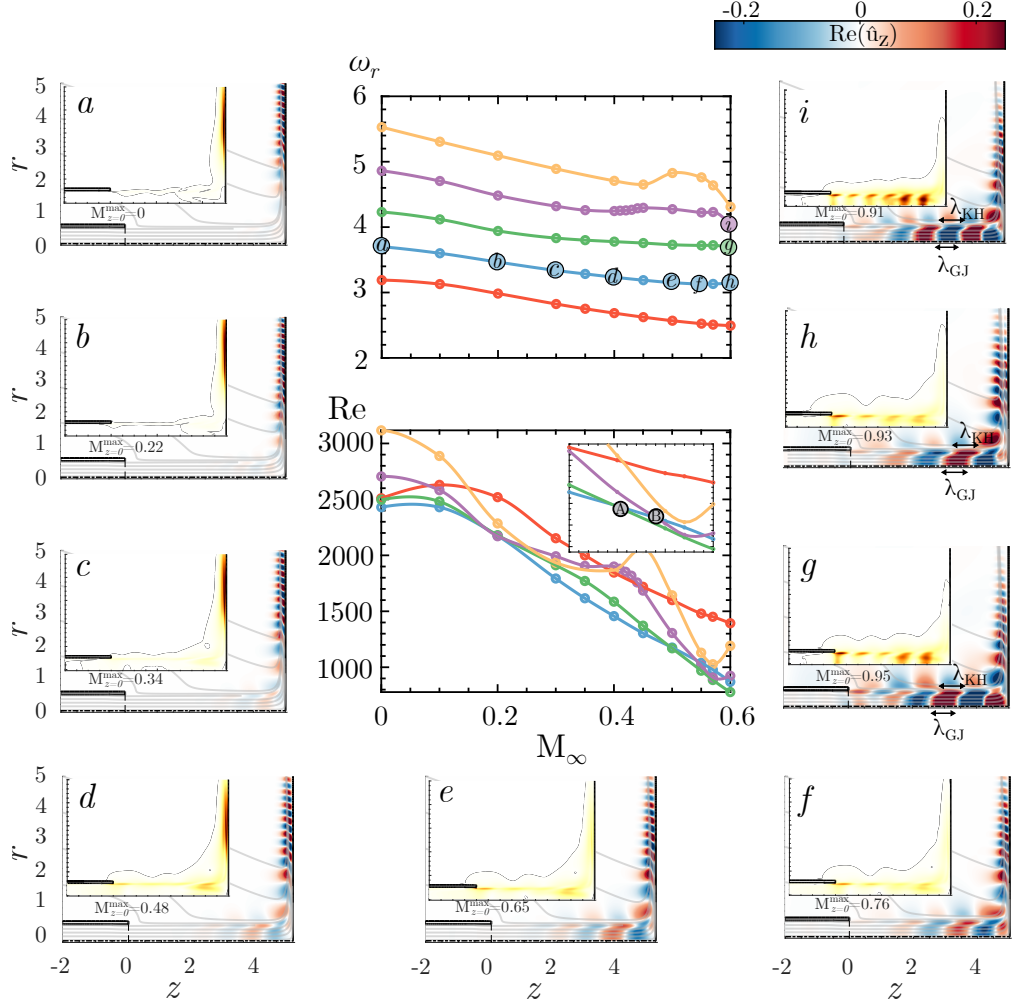


Figure 3: Bifurcation diagram showing the neutral curves of stability and evolution of the critical pulsation ω_r of the axisymmetric steady-state flow for a nozzle to wall distance $H/D = 5$. Visualization of the critical eigenmode (real part of the axial velocity) with overlaid steady-flow streamlines. Each visualization contains a superposed image of the structural sensitivity map.

process and occurs within the interacting region between the axial and radial shear layers, i.e. $4.5D < z < H$.

The primary instability corresponds to a Hopf bifurcation, leading to a periodic solution with $\omega \approx 3.7$ (blue line in fig. 3) for $M_\infty < 0.49$ and to frequency $\omega \approx 4$ (green line in the figure) for $M_\infty > 0.49$. The mode switching happens in a codimension Hopf-Hopf two point, which it has also been experimentally observed in Nosseir & Ho (1982), where they also detected hysteresis-like behaviour between two modes.

The non-local feedback mechanism selects the frequency of the global mode for every Mach number, however the strength of the feedback loop rapidly decreases with the Mach number. This feature may be observed directly from the global modes by comparing the ones obtained at large subsonic Mach number ($M_\infty = 0.6$, $M_J \approx 0.9$) represented by

subfigures (g-i) and the ones for lower Mach numbers, see subfigures (a-f). Please note that the amplitude of the modes is normalised in such a way that the perturbation energy (Chu 1965) is unitary.

Figure 3 also displays, in an inset located at the upper left location of each subfigure, the structural sensitivity, introduced by Giannetti & Luchini (2007) and defined herein in section 4.1. The structural sensitivity highlights the spatial location where a generic modification of the instability core produces the largest drift in the growth rate or frequency of the mode. Therefore, it is hereafter considered as the core of the instability. For large subsonic Mach numbers ($0.5 < M_\infty < 0.6$) the structural sensitivity has an extended compact support within the axial shear layer and the jet region. It is intermittent, located at the axial position of the pulses in the axial shear layer of the direct mode, excluding the region near the wall ($H - D < z < H$). Thus, suggesting that the region near the wall does not play a dominant effect to the instability at large Mach number. Tentatively, one can argue the following about the two types of peaks of the structural sensitivity. The dominant peaks of the structural sensitivity at the shear-layer correspond to the energy transfers between the baseflow shear and the perturbation. And the large amplitude peaks within the jet may be the region where the vortical fluctuations are transformed into acoustics via a coupling mechanism. It may be observed from fig. 4 (a) that the region of largest divergence of the mode matches with the spatial location highlighted by the structural sensitivity. One can determine the production of fluctuating divergence from the divergence of the linearised momentum equation, that is,

$$\begin{aligned}
 & \overbrace{-i\omega \nabla \cdot \hat{\mathbf{u}} + \mathbf{u}_0 \cdot \nabla (\nabla \cdot \hat{\mathbf{u}}) + \nabla \cdot \left(\frac{\hat{\rho}}{\rho_0} \mathbf{u}_0 \cdot \nabla \mathbf{u}_0 \right)}^{C_A^{\text{div}}} = -\overbrace{\hat{\mathbf{u}} \cdot \nabla (\nabla \cdot \mathbf{u}_0)}^{C_{P,b}^{\text{div}}} - \overbrace{\frac{\Delta \hat{\rho}}{\rho_0} + \frac{\nabla \hat{\rho} \cdot \nabla \rho_0}{\rho_0^2}}^{P_a^{\text{div}}} \\
 & \quad - \underbrace{\left((\nabla \hat{\mathbf{u}})^T : \nabla \mathbf{u}_0 + (\nabla \mathbf{u}_0)^T : \nabla \hat{\mathbf{u}} \right)}_{C_{P,a}^{\text{div}}} \\
 & \quad + \underbrace{\frac{1}{\text{Re}} \nabla \cdot (\nabla \cdot \tau(\hat{\mathbf{u}}))}_{P_b^{\text{div}}} \tag{3.1a}
 \end{aligned}$$

Note that, eq. (3.1) can be written entirely in terms of velocity and density fluctuations, if we assume that the pressure fluctuations are isentropic, i.e., $M_\infty^2 \hat{p} = \hat{\rho} T_0$. The module of the convection term, hereafter referred to as C_A^{div} corresponds to the convection of the divergence and density fluctuations by the baseflow. This term is displayed in fig. 4 (b). The spatial support of C_A^{div} lies within the jet region and the radial shear layer. Nonetheless, despite the fact that it is supported at the location of the maximum fluctuating divergence, one cannot associate this term as a source of divergence production. It merely advects fluctuating divergence and density, that has been already produced within the flow. The spatial support of term $C_{P,a}^{\text{div}}$, displayed in fig. 4 (d), mostly lies within the shear layer and in regions with non-zero divergence of the baseflow (not shown). P_a^{div} is the pressure source term whose spatial support lies in the shear layer, in a region within the jet near the wall ($H - D < z < H$) and the region near the nozzle exit. The largest local contribution to the fluctuating divergence is due to this term. The other two production terms ($C_{P,b}^{\text{div}}$ and P_b^{div}) are of small magnitude, and their spatial support is not found within the region of the maximum of the divergence. However, we have previously argued that the pressure, if we assume an isentropic process at the perturbation level, plays a similar role to the one of the density. Tentatively, one

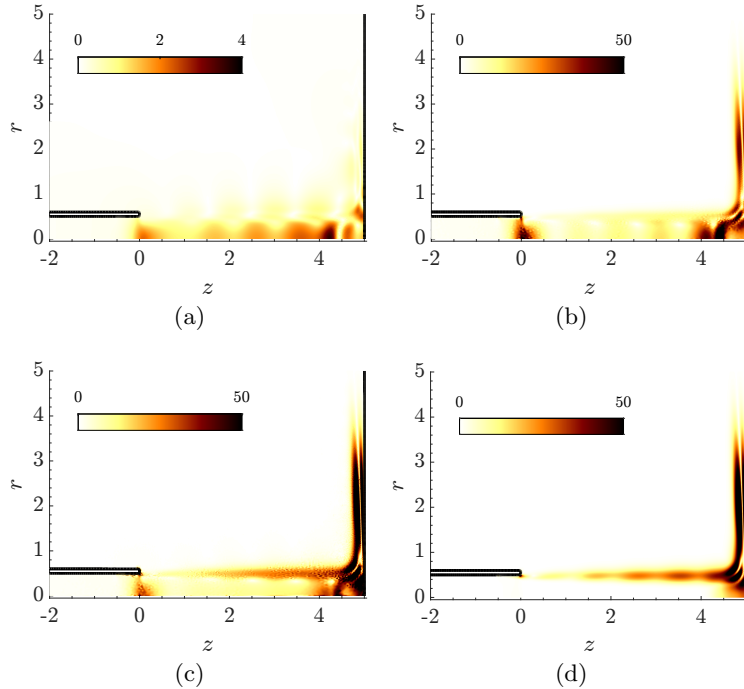


Figure 4: Module of the (a) divergence of the mode; (b) module of the term C_A^{div} in eq. (3.1a); (c) module of the term P_a^{div} in eq. (3.1a); (d) module of the term $C_{P,a}^{\text{div}}$ in eq. (3.1a).

may argue that the pressure serves to enforce the continuity condition, thereby inducing a modification of the volume flux. In a similar way, by taking the material derivative of the linearised continuity equation, it is possible to derive a generalised wave equation, where the dominant source term is a term proportional to the fluctuating divergence (not shown here). Then, we could say that in a second step, the divergence of the mode induces an acoustic pulse that is propagated as a longitudinal density wave, and therefore providing the closure of the feedback-loop.

On the other hand, for low subsonic Mach numbers ($M_\infty < 0.4$), the structural sensitivity has an extended support within the radial shear layer ($2.5D < r < 5D$). In this case, the structural sensitivity has a thin continuous structure. To understand the nature of the wavemaker at low Mach numbers, we write the linearised momentum equation in the Crocco's form (Rienstra & Hirschberg 2004),

$$-\mathrm{i}\omega\hat{\mathbf{u}} + \nabla \cdot \left((\mathbf{u}_0 \cdot \hat{\mathbf{u}} + \frac{\hat{p}}{\rho_0})\mathbf{I} - \boldsymbol{\tau}(\hat{\mathbf{u}}) \right) = \mathbf{u}_0 \times \hat{\boldsymbol{\omega}} + \hat{\mathbf{u}} \times \boldsymbol{\omega}_0, \quad (3.2)$$

where we have neglected the term $-\frac{\nabla \rho_0 \hat{p}}{\rho_0^2}$, which is of small magnitude at low Mach number. We can readily observe that the linearised Lamb vector $\mathbf{u}_0 \times \hat{\omega} + \hat{\mathbf{u}} \times \omega_0$ acts as a source term, and one could argue that it corresponds first to the region driving the hydrodynamic instability, and second to a source of sound, which is in turn, responsible for the production of the backward propagating acoustic pressure that closes the feedback-loop (Powell 1990; Howe 1975). Figure 5 displays the linearised Lamb vector, which is localised within the radial shear layer and at the same spatial location as the structural sensitivity

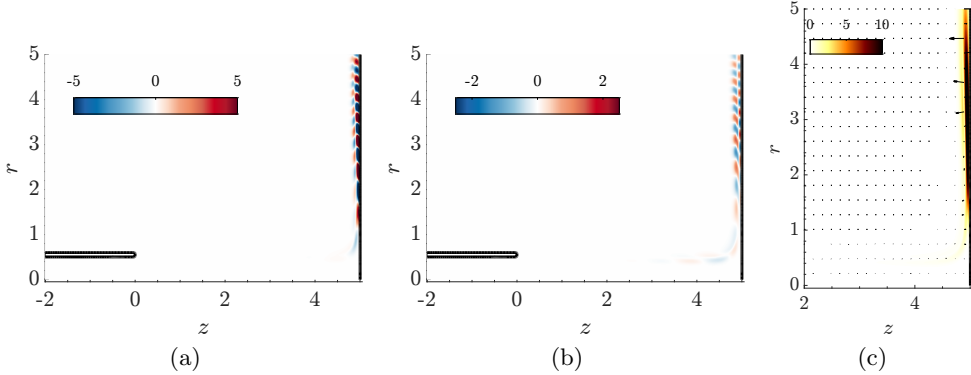


Figure 5: (a-b) Axial and radial components, respectively, of the real part of the linearised Lamb vector $\mathbf{u}_0 \times \hat{\omega} + \hat{\mathbf{u}} \times \omega_0$ at $M_\infty = 0.2$ and $Re = 2200$. (c) Module of the Lamb vector, the arrows indicate the direction.

at low Mach numbers. Thus, providing a rationalisation to the nature of the wavemaker, which in this situation is located along the vortex sheet near the impinging wall. For the sake of consistency, please note that the Lamb vector at large Mach numbers also possess a similar structure, that is, it is a thin-elongated structure along the vortex sheet (not shown). However, the structural sensitivity does not have this kind of structure, thus suggesting that vortex sound is not the dominant vortical-acoustic coupling.

4. Decomposition of the feedback mechanism

In order to gain a better understanding of the feedback process responsible for the instability, we perform two types of decomposition. First, a Helmholtz-Hodge decomposition of the global linear mode $\hat{\mathbf{q}}$, which allows distinguishing between the acoustic and vortical+entropic components of the flow. Additionally, such a decomposition allows us to formulate a finer *structural sensitivity* concept. This decomposition of the structural sensitivity highlights the space location where a vortical (resp. acoustic) modification in the structure of the problem is able to produce the greatest drift in the eigenvalue of the operator projected onto the acoustic or vortical component. The study is then pursued with the analysis of the feedback-loop with the *endogeneity* map, which provides further access to the relation between the growth rate or frequency of the mode in terms of underlying the physical mechanisms. We finish the section with a decomposition of the global mode in terms of the local waves underpinned by the baseflow, which allows us to determine the reflection coefficient between the shear layer wave and the guided jet wave at neutrality.

4.1. Decomposition of the linear perturbation

The linear perturbation $\hat{\mathbf{q}}$ is herein decomposed into three components: *acoustic*, *hydrodynamic* and *entropic*. There is a large literature in decomposition of acoustic sources (Ewert & Schröder 2003; Spieser 2020) to compute acoustic propagation effects. In our case, we follow the reciprocal reasoning, we adopt a monolithic computation of the compressible flow, i.e. we do not decompose the flow in acoustic sources and acoustic propagation, and we would like to unveil the feedback loop responsible for the instability mechanism and the frequency selection.

For this purpose, we adopt a Helmholtz-Hodge decomposition (Schoder *et al.* 2020) of

the perturbation velocity field into *acoustic* (potential) and *hydrodynamic* (solenoidal)

$$\hat{\mathbf{u}} = \hat{\mathbf{u}}_{\text{ac}} + \hat{\mathbf{u}}_{\text{hyd}} = \nabla\phi_c + \nabla \times \Psi \quad (4.1)$$

applying divergence to eq. (4.1), the potential ϕ_c is determined from the following Poisson equation

$$\begin{aligned} \Delta\phi_c &= \nabla \cdot \hat{\mathbf{u}} && \text{in } \Omega \\ \nabla\phi_c \cdot \mathbf{n} &= \hat{\mathbf{u}} \cdot \mathbf{n} && \text{on } \partial\Omega. \end{aligned} \quad (4.2)$$

The hydrodynamic component of the velocity is subsequently determined by subtracting $\hat{\mathbf{u}}_{\text{hyd}} = \hat{\mathbf{u}} - \hat{\mathbf{u}}_{\text{ac}} = \hat{\mathbf{u}} - \nabla\phi_c$. Note that, the uniqueness of the Helmholtz decomposition is subjected to the L^2 -orthogonality condition, in our case satisfied by the suitable boundary condition of eq. (A 6), and the decay of the velocity field at the far-field (Schoder *et al.* 2020).

The pressure component of the mode $\hat{\mathbf{q}}$ is determined from the momentum equation

$$-\frac{1}{\rho_0} \nabla \hat{p} = i\omega \hat{\mathbf{u}} + \hat{\mathbf{u}} \cdot \nabla \mathbf{u}_0 + \mathbf{u}_0 \cdot \nabla \hat{\mathbf{u}} + \frac{\hat{\rho}}{\rho_0} \mathbf{u}_0 \cdot \nabla \mathbf{u}_0 - \frac{1}{\text{Re}} \nabla \cdot \tau(\hat{\mathbf{u}}), \quad (4.3)$$

from the decomposition $\hat{p} = \hat{p}_{\text{ac}} + \hat{p}_{\text{hyd}} + \hat{p}_{\text{s}}$ and applying the divergence operator to the momentum equation, we obtain the following equations

$$\begin{aligned} -\frac{1}{\rho_0} \Delta \hat{p}_{\text{ac}} + \frac{\nabla \rho_0 \cdot \nabla \hat{p}_{\text{ac}}}{\rho_0^2} - \nabla \cdot \left(\frac{M_\infty^2}{T_0} (\mathbf{u}_0 \cdot \nabla \mathbf{u}_0) \frac{\hat{p}_{\text{ac}}}{\rho_0} \right) &= i\omega \nabla \cdot \hat{\mathbf{u}}_{\text{ac}} + \nabla \cdot (\mathbf{u}_0 \cdot \nabla \hat{\mathbf{u}}_{\text{ac}}) \\ &\quad + \nabla \cdot (\hat{\mathbf{u}}_{\text{ac}} \cdot \nabla \mathbf{u}_0) \end{aligned} \quad (4.4a)$$

$$\begin{aligned} -\frac{1}{\rho_0} \Delta \hat{p}_{\text{hyd}} + \frac{\nabla \rho_0 \cdot \nabla \hat{p}_{\text{hyd}}}{\rho_0^2} - \nabla \cdot \left(\frac{M_\infty^2}{T_0} (\mathbf{u}_0 \cdot \nabla \mathbf{u}_0) \frac{\hat{p}_{\text{hyd}}}{\rho_0} \right) &= \nabla \cdot (\mathbf{u}_0 \cdot \nabla \hat{\mathbf{u}}_{\text{hyd}}) \\ &\quad + \nabla \cdot (\hat{\mathbf{u}}_{\text{hyd}} \cdot \nabla \mathbf{u}_0) \end{aligned} \quad (4.4b)$$

with decay at the far-field $r \rightarrow \infty$. Details of the derivation are given in appendix A.1. Finally, the entropic part of the pressure is recovered by subtracting the two other components to the pressure of the mode $\hat{p}_{\text{s}} = \hat{p} - \hat{p}_{\text{ac}} - \hat{p}_{\text{hyd}}$, which accounts for the dissipation effects of the viscous stress-tensor.

The other two components, temperature and density, are determined as follows. The acoustic and hydrodynamic components are considered to evolve isentropically and are directly determined from the pressure,

$$\hat{T}_{\text{ac}} = (\gamma - 1) M_\infty^2 \hat{p}_{\text{ac}}, \quad \hat{T}_{\text{hyd}} = (\gamma - 1) M_\infty^2 \hat{p}_{\text{hyd}}, \quad \hat{T}_{\text{s}} = \hat{T} - \hat{T}_{\text{ac}} - \hat{T}_{\text{hyd}}, \quad (4.5)$$

$$\hat{\rho}_{\text{ac}} = M_\infty^2 \frac{\rho_0}{T_0} \hat{p}_{\text{ac}}, \quad \hat{\rho}_{\text{hyd}} = M_\infty^2 \frac{\rho_0}{T_0} \hat{p}_{\text{hyd}}, \quad \hat{\rho}_{\text{s}} = \hat{\rho} - \hat{\rho}_{\text{ac}} - \hat{\rho}_{\text{hyd}}. \quad (4.6)$$

Let us illustrate the application of this decomposition to a particular example. For that purpose, we have chosen the global mode (h) of fig. 3. Figure 6 depicts the components of the density fluctuations $\hat{\rho}$. The hydrodynamic density fluctuations $\hat{\rho}_{\text{hyd}}$, being only hydrodynamic, resemble to the hydrodynamic pressure fluctuations, which result from a Kelvin-Helmholtz instability of the shear layer, at low Mach numbers (Sierra-Ausin *et al.* 2022). The entropic component of the density $\hat{\rho}_{\text{s}}$, which is illustrated in (c), is localised within the shear layer. In this component, one can perfectly appreciate the wavelength and the number of nodes of forward wave composing the feedback loop, in this case the forward wave has six nodes. The acoustic component of the density $\hat{\rho}_{\text{ac}}$, depicted in (a), is composed of a radiating part and the guided jet wave, which is localised within the jet region. In this case, the guided jet wave is composed of two waves, i.e. it has four nodes. From this decomposition, we can formulate a criterion for the frequency selection,

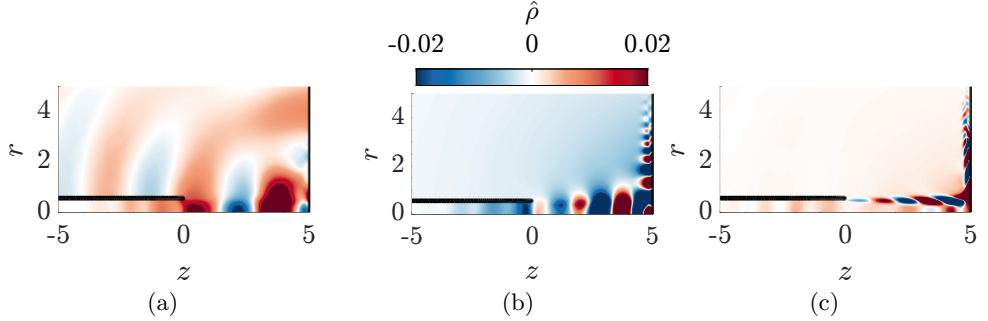


Figure 6: Density decomposition of the global mode with $St \approx 0.5$ at criticality ($Re = 900$) at $M_\infty = 0.6$ (Mode (h) in fig. 3). (a) Acoustic component of density $\hat{\rho}_{ac}$. (b) Hydrodynamic component of density $\hat{\rho}_{hyd}$. (c) Entropic component of density $\hat{\rho}_s$

similar to the Rössiter modes,

$$St^{-1} = \frac{H/D}{U_{c,SL} n_{hyd}} + \frac{H/D}{M_\infty^{-1} n_{ac}}, \text{ with } U_{c,SL} \approx \frac{1}{2} U_{r=0} \quad (4.7)$$

such a criterion considers that the phase velocity of the hydrodynamic forward mode corresponds to the inviscid approximation, that is, $U_{c,SL}$ takes the mean value between the two velocities of the shear layer, and the guided jet wave is propagated back nearly at the speed of sound of the far-field. Such a criterion provides a way to classify the global modes from the number of half-wavelengths of the guided jet wave mode (n_{ac}) and the hydrodynamic mode (n_{hyd}).

4.2. Non-local structural sensitivity decomposition

The global instability is caused by a feedback process between two travelling waves, which impedes a direct *local* definition of the *wavemaker* or *structural sensitivity*. That is, we can still formulate the concept of structural sensitivity, but it is no longer localised in space, i.e., it displays a support all along the interacting path between the two travelling waves. We briefly recall the concept of structural sensitivity, before introducing an adequate decomposition of the wavemaker for global instabilities generated by non-local feedback process. The adjoint equations are herein used to evaluate the effect of a linear harmonic forcing $\mathbf{H}(\hat{\mathbf{q}}) \equiv \delta(\mathbf{x} - \mathbf{x}_0) \mathbf{P}_\mathbf{H} \mathbf{C}_0 \mathbf{P}_{\hat{\mathbf{q}}} \hat{\mathbf{q}}$,

$$\left(-i\omega \mathbf{B}|_{\mathbf{q}_0} + \mathbf{D}\mathbf{F}|_{\mathbf{q}_0} \right) \hat{\mathbf{q}} = \mathbf{H}(\hat{\mathbf{q}}). \quad (4.8)$$

\mathbf{C}_0 is a generic linear operator acting on $\hat{\mathbf{q}}$, and $\mathbf{P}_\mathbf{H}$ a diagonal matrix that selects the type of forcing. In the following, we neglect mass injection to the system, and we simply consider momentum forcing and a source of heat release, that is, $\mathbf{P}_\mathbf{H} = \text{diag}(0, \mathbf{I}, 1, 0, 0)$. The projection operator $\mathbf{P}_{\hat{\mathbf{q}}}$ is also a diagonal matrix that selects the dependency of the forcing on the perturbation. The structural sensitivity tensor is therefore defined as

$$i\delta\omega = \langle \mathbf{P}_\mathbf{H} \hat{\mathbf{q}}^\dagger, \delta(\mathbf{x} - \mathbf{x}_0) \mathbf{C}_0 \mathbf{P}_{\hat{\mathbf{q}}} \hat{\mathbf{q}} \rangle \leq ||\mathbf{C}_0|| ||\mathbf{P}_\mathbf{H} \hat{\mathbf{q}}^\dagger||_{L^2} ||\mathbf{P}_{\hat{\mathbf{q}}} \hat{\mathbf{q}}||_{L^2} = ||\mathbf{C}_0|| \mathbf{S}_s(\mathbf{x}_0), \quad (4.9)$$

that is, the structural sensitivity map is defined as $\mathbf{S}_s(\mathbf{x}_0) \equiv ||\mathbf{P}_\mathbf{H} \hat{\mathbf{q}}^\dagger||_{L^2} ||\mathbf{P}_{\hat{\mathbf{q}}} \hat{\mathbf{q}}||_{L^2}$. The scalar field \mathbf{S}_s is then an upper bound function for the eigenvalue variation, and it can be employed to determine locations where the feedback is stronger. Therefore, allowing an identification of the regions where the instability mechanism acts. However, when it is not localized within a small physical region, it does not clearly identify the *wavemaker*,

but a possible interacting region between the components of the global mode.

Decomposing the mode $\hat{\mathbf{q}}$ we can rewrite the harmonic forcing as $\mathbf{H}(\hat{\mathbf{q}}) = \mathbf{H}(\hat{\mathbf{q}}_{\text{ac}} + \hat{\mathbf{q}}_{\text{hyd}} + \hat{\mathbf{q}}_s)$, which due to linearity of the forcing term on the eigenmode is simply expressed as

$$\mathbf{H}(\hat{\mathbf{q}}) = \mathbf{H}(\hat{\mathbf{q}}_{\text{ac}}) + \mathbf{H}(\hat{\mathbf{q}}_{\text{hyd}}) + \mathbf{H}(\hat{\mathbf{q}}_s). \quad (4.10)$$

Thus, we have a first decomposition of the harmonic forcing $\mathbf{H}(\hat{\mathbf{q}})$ from the splitting of the state variable. However, the term $\mathbf{H}(\hat{\mathbf{q}}_{\text{ac}})$ is not necessarily a forcing term that uniquely induces acoustic perturbations. Assume, for simplicity, that the previous forcing term depends uniquely on the acoustic velocity, $\mathbf{H}(\mathbf{u}_{\text{ac}})$, and it only acts on the momentum equation, that is, we neglect mass or heat injection. The forcing term must be rotational-free, i.e., $\nabla \times \mathbf{H}(\mathbf{u}_{\text{ac}}) = 0$, otherwise it will induce vortical perturbations into the flow. Therefore, $\mathbf{H}(\hat{\mathbf{q}}_{\text{ac}})$ should be interpreted as a generic forcing term that depends on the acoustic perturbation. To determine the effect of the forcing, that is, which kind of response induces, we decompose the forcing operator into $\mathbf{H} = \mathbf{H}_{\text{ac}} + \mathbf{H}_{\text{hyd}} + \mathbf{H}_s$ as in section 4.1. Following, this reasoning, we decompose eq. (4.11),

$$\begin{aligned} \left(-i\omega \mathbf{B}|_{\mathbf{q}_0} + \mathbf{DF}|_{\mathbf{q}_0} \right) \hat{\mathbf{q}}_{\text{ac}} &= \mathbf{H}_{\text{ac}}(\hat{\mathbf{q}}_{\text{ac}}) + \mathbf{H}_{\text{ac}}(\hat{\mathbf{q}}_{\text{hyd}}) + \mathbf{H}_{\text{ac}}(\hat{\mathbf{q}}_s), \\ \left(-i\omega \mathbf{B}|_{\mathbf{q}_0} + \mathbf{DF}|_{\mathbf{q}_0} \right) \hat{\mathbf{q}}_{\text{hyd}} &= \mathbf{H}_{\text{hyd}}(\hat{\mathbf{q}}_{\text{ac}}) + \mathbf{H}_{\text{hyd}}(\hat{\mathbf{q}}_{\text{hyd}}) + \mathbf{H}_{\text{hyd}}(\hat{\mathbf{q}}_s), \\ \left(-i\omega \mathbf{B}|_{\mathbf{q}_0} + \mathbf{DF}|_{\mathbf{q}_0} \right) \hat{\mathbf{q}}_s &= \mathbf{H}_s(\hat{\mathbf{q}}_{\text{ac}}) + \mathbf{H}_s(\hat{\mathbf{q}}_{\text{hyd}}) + \mathbf{H}_s(\hat{\mathbf{q}}_s). \end{aligned} \quad (4.11)$$

The interpretation of the adjoint $\hat{\mathbf{q}}^\dagger$ as a measure of the receptivity with respect to a harmonic forcing allows us to decompose the adjoint in a similar manner to the way we decomposed the global mode in section 4.1. In this manner, the adjoint variable serves to project the forcing term onto each of the subspaces with the decomposed adjoint $\hat{\mathbf{q}}^\dagger = \hat{\mathbf{q}}_{\text{ac}}^\dagger + \hat{\mathbf{q}}_{\text{hyd}}^\dagger + \hat{\mathbf{q}}_s^\dagger$. That is, $\mathbf{H}_{\text{ac}}(\hat{\mathbf{q}}) = \langle \hat{\mathbf{q}}_{\text{ac}}^\dagger, \mathbf{H}(\hat{\mathbf{q}}) \rangle \hat{\mathbf{q}}_{\text{ac}}$, $\mathbf{H}_{\text{hyd}}(\hat{\mathbf{q}}) = \langle \hat{\mathbf{q}}_{\text{hyd}}^\dagger, \mathbf{H}(\hat{\mathbf{q}}) \rangle \hat{\mathbf{q}}_{\text{hyd}}$ and $\mathbf{H}_s(\hat{\mathbf{q}}) = \langle \hat{\mathbf{q}}_s^\dagger, \mathbf{H}(\hat{\mathbf{q}}) \rangle \hat{\mathbf{q}}_s$. Then, we can rewrite eq. (4.11),

$$\begin{aligned} \left(-i\omega \mathbf{B}|_{\mathbf{q}_0} + \mathbf{DF}|_{\mathbf{q}_0} + \langle \hat{\mathbf{q}}_{\text{ac}}^\dagger, \mathbf{H}(\hat{\mathbf{q}}_{\text{ac}}) \rangle + \langle \hat{\mathbf{q}}_{\text{ac}}^\dagger, \mathbf{H}(\hat{\mathbf{q}}_{\text{hyd}}) \rangle + \langle \hat{\mathbf{q}}_{\text{ac}}^\dagger, \mathbf{H}(\hat{\mathbf{q}}_s) \rangle \right) \hat{\mathbf{q}}_{\text{ac}} &= 0 \\ \left(-i\omega \mathbf{B}|_{\mathbf{q}_0} + \mathbf{DF}|_{\mathbf{q}_0} + \langle \hat{\mathbf{q}}_{\text{hyd}}^\dagger, \mathbf{H}(\hat{\mathbf{q}}_{\text{ac}}) \rangle + \langle \hat{\mathbf{q}}_{\text{hyd}}^\dagger, \mathbf{H}(\hat{\mathbf{q}}_{\text{hyd}}) \rangle + \langle \hat{\mathbf{q}}_{\text{hyd}}^\dagger, \mathbf{H}(\hat{\mathbf{q}}_s) \rangle \right) \hat{\mathbf{q}}_{\text{hyd}} &= 0 \\ \left(-i\omega \mathbf{B}|_{\mathbf{q}_0} + \mathbf{DF}|_{\mathbf{q}_0} + \langle \hat{\mathbf{q}}_s^\dagger, \mathbf{H}(\hat{\mathbf{q}}_{\text{ac}}) \rangle + \langle \hat{\mathbf{q}}_s^\dagger, \mathbf{H}(\hat{\mathbf{q}}_{\text{hyd}}) \rangle + \langle \hat{\mathbf{q}}_s^\dagger, \mathbf{H}(\hat{\mathbf{q}}_s) \rangle \right) \hat{\mathbf{q}}_s &= 0, \end{aligned} \quad (4.12)$$

which exemplifies the role of the decomposed adjoint variable to project the structural forcing perturbation onto the corresponding subspace.

An inspection of eq. (4.12) suggests the definition of a *non-local structural sensitivity* matrix as

$$\begin{aligned} i\delta\omega_j^k &= \langle \hat{\mathbf{q}}_k^\dagger, \delta(\mathbf{x} - \mathbf{x}_0) \mathbf{C}_0 \hat{\mathbf{q}}_j \rangle \leq \|\mathbf{C}_0\| \|\hat{\mathbf{q}}_k^\dagger(\mathbf{x}_0)\| \|\hat{\mathbf{q}}_j(\mathbf{x}_0)\| = \|\mathbf{C}_0\| \mathbf{S}^{(j,k)}_s(\mathbf{x}_0), \\ \mathbf{S}^{(j,k)}_s(\mathbf{x}_0) &= \|\hat{\mathbf{q}}_k^\dagger(\mathbf{x}_0)\| \|\hat{\mathbf{q}}_j(\mathbf{x}_0)\| \text{ with } j, k = \text{ac, hyd, s}. \end{aligned} \quad (4.13)$$

The new *structural sensitivity* provides information about the cross-interaction between vortical and acoustic components of the flow. In the problem of the impinging jet, the feedback loop is initiated by the hydrodynamic instability of the shear layer, which induces an acoustic response. In turn, when acoustic wave impinges on the nozzle lip promotes back the hydrodynamic instability, continuing the loop. With this novel definition, $\mathbf{S}_s^{(hyd,ac)}$ identifies the most sensitive region of the flow to vortical perturbations, inducing an acoustic response. This first region can be named the wavemaker of the hydrodynamic perturbations exciting an acoustic response, which in the case of the impinging jet is expected to be located near the impinging wall and possibly near sharp corners. The second (and third) wavemaker of interest corresponds to the excitation

of a hydrodynamic response from hydrodynamic ($\mathbf{S}_s^{(hyd,hyd)}$) or acoustic perturbations ($\mathbf{S}_s^{(ac,hyd)}$). Physically, $\mathbf{S}_s^{(hyd,hyd)}$ determines the hydrodynamic wavemaker, which in a causal reasoning, could be argued to be the region initiating the feedback process. And $\mathbf{S}_s^{(ac,hyd)}$ determines the most sensitive region of the flow to an acoustic perturbation inducing a hydrodynamic excitation, that is, the retro-action of the acoustic wave into the hydrodynamic instability. Additionally, we introduce a further decomposition of the non-local structural sensitivity map to account only for the forcing of the momentum equation for a forcing term that depends uniquely on the velocity field, that is,

$$\begin{aligned} i\delta\omega_j^k &= \langle \hat{\mathbf{u}}_k^\dagger, \delta(\mathbf{x} - \mathbf{x}_0) \mathbf{C}_0 \hat{\mathbf{u}}_j \rangle \leq \|\mathbf{C}_0\| \|\hat{\mathbf{u}}_k^\dagger(\mathbf{x}_0)\| \|\hat{\mathbf{u}}_j(\mathbf{x}_0)\| = \|\mathbf{C}_0\| \mathbf{S}_{\hat{\mathbf{u}},s}^{(j,k)}(\mathbf{x}_0), \\ \mathbf{S}_{\hat{\mathbf{u}},s}^{(j,k)}(\mathbf{x}_0) &= \|\hat{\mathbf{u}}_k^\dagger(\mathbf{x}_0)\| \|\hat{\mathbf{u}}_j(\mathbf{x}_0)\| \text{ with } j, k = \text{ac, hyd, s}. \end{aligned} \quad (4.14)$$

We are left with the decomposition of the adjoint eigenmode. Herein, we summarise the decomposition, a detailed derivation is left to appendix A.2. We propose the following decomposition for the adjoint velocity field,

$$\begin{aligned} \hat{\mathbf{u}}^\dagger &= \hat{\mathbf{u}}_{\text{hyd}}^\dagger + \hat{\mathbf{u}}_{\text{ac}}^\dagger = \nabla\phi_c^\dagger + \nabla \times \Psi^\dagger, \\ \Delta\phi_c^\dagger &= \nabla \cdot \hat{\mathbf{u}}^\dagger \text{ in } \Omega \\ \nabla\phi_c^\dagger \cdot \mathbf{n} &= \hat{\mathbf{u}}^\dagger \cdot \mathbf{n} \text{ on } \partial\Omega. \end{aligned} \quad (4.15)$$

From eq. (4.9), we can interpret the adjoint variable as the sensitivity of the eigenvalue/eigenvector variations with respect to a linear harmonic forcing. In this sense, $\hat{\mathbf{u}}_{\text{ac}}^\dagger$ corresponds to the sensitivity to vortical-free eigenvector variations with respect to a generic linear harmonic forcing in the momentum equation. Similarly, $\hat{\mathbf{u}}_{\text{hyd}}^\dagger$ should be understood as the sensitivity to the dilation-free eigenvector variations with respect to a generic linear harmonic forcing in the momentum equation.

When considering the adjoint variables, we prefer to consider the evolution equation of the entropy fluctuations \hat{s} instead of the energy equation, see appendix A for the introduction of the linearised governing equations in entropy-form. The inclusion of a source term into the entropy equation, for instance a source of heat release, induces a modification of the entropy evolution. By definition, we defined hydrodynamic and acoustic modes to be isentropic (we neglected the effects of viscous dissipation), thus \hat{s}^\dagger projects sources in the entropy equation to sources of entropic nature, i.e., $\hat{s}^\dagger = \hat{s}_s^\dagger$, a trivial decomposition. Instead, source terms in the energy equation may induce modifications of the acoustic and hydrodynamic components of the flow, and its decomposition is more cumbersome. Finally, the decomposition of the adjoint of the continuity equation, $\hat{\rho}^\dagger$, is determined by substituting the previously decomposed adjoint and entropy adjoint fields into the linearised adjoint equations, which is left to appendix A.2. Overall, the adjoint is decomposed as follows,

$$\begin{aligned} \hat{\mathbf{u}}^\dagger &= \hat{\mathbf{u}}_{\text{hyd}}^\dagger + \hat{\mathbf{u}}_{\text{ac}}^\dagger = \nabla\phi_c^\dagger + \nabla \times \Psi^\dagger, \text{ from eq. (4.15)} \\ \hat{s}^\dagger &= \hat{s}_s^\dagger \\ \hat{\rho}^\dagger &= \hat{\rho}_{\text{ac}}^\dagger + \hat{\rho}_{\text{hyd}}^\dagger + \hat{\rho}_s^\dagger, \text{ from eq. (A 14)} \\ \hat{p}^\dagger &= \hat{p}_{\text{ac}}^\dagger = \frac{\nabla \cdot \hat{\mathbf{u}}^\dagger}{\gamma M_\infty^2} \\ \hat{T}^\dagger &= \hat{T}_{\text{ac}}^\dagger + \hat{T}_s^\dagger = -\frac{\nabla \cdot \hat{\mathbf{u}}^\dagger}{\gamma M_\infty^2} + (\hat{s}^\dagger \mathbf{u}_0 \cdot \nabla s_0 - \frac{\gamma}{\text{Pr Re}} \frac{1}{\rho_0} \Delta s_0) \end{aligned} \quad (4.16)$$

An important property of the adjoint-direct mode bases is the bi-orthogonality. The pairs of primitive variables $\{0, \hat{\mathbf{u}}, \hat{s}\}; (0, \hat{\mathbf{u}}^\dagger, \hat{s})$ are bi-orthogonal, but that is no longer

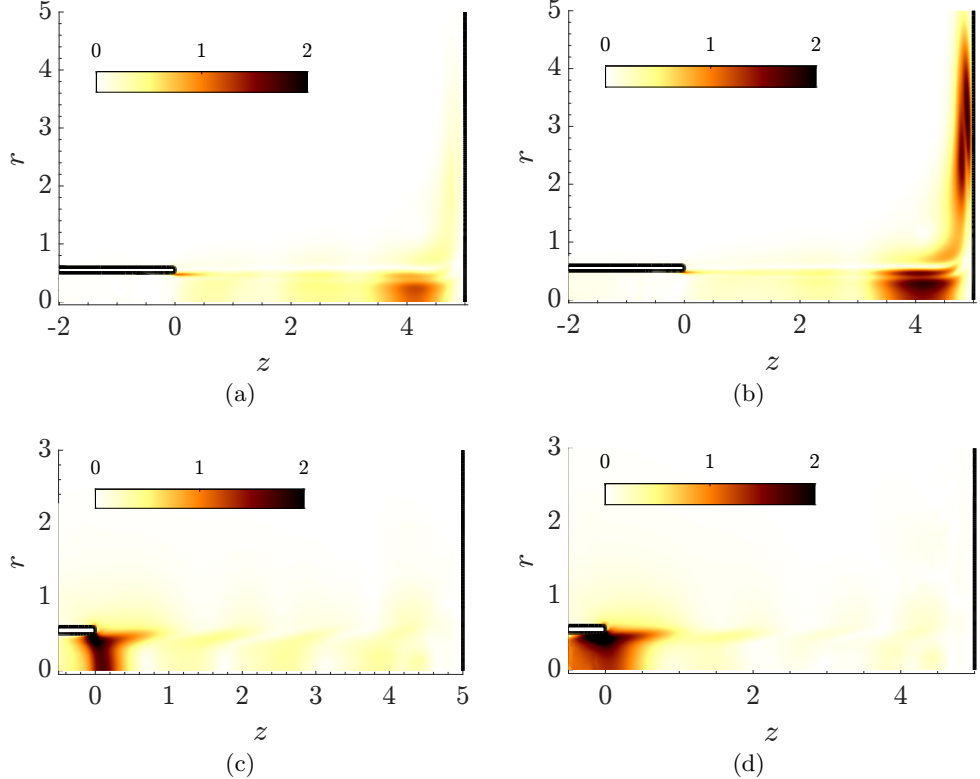


Figure 7: (a-b) Map $\mathbf{S}_{\mathbf{u},s}^{(hyd,ac)}$ for the global mode of points (h) and (e) of fig. 3. (c-d) Map $\mathbf{S}_{\mathbf{u},s}^{(ac,hyd)}$ for the global mode of points (h) and (e) of fig. 3.

true when considering the complete primitive variable $\{(\hat{\rho}, \hat{\mathbf{u}}, \hat{s}); (\hat{\rho}^\dagger, \hat{\mathbf{u}}^\dagger, \hat{s})\}$, that is, when considering the continuity equation or the density variable. The set of bases lacks the bi-orthogonality property when mass is injected to the system, which implies the existence of an intrinsic coupling mechanism between the three components of the mode via the continuity equation. Which, in turn, impedes the decomposition of the sources of mass as acoustic, hydrodynamic or entropic. In the following, we will restrict ourselves to sources in the momentum equation, that is, we use eq. (4.14) to analyse the response of the system to body forces. Figure 7 displays two pairs of structural sensitivity pairs. The first, $\mathbf{S}_{\mathbf{u},s}^{(hyd,ac)}$, is the map measuring the eigenvalue drift due to an acoustic response induced by a hydrodynamic perturbation. At large Mach numbers ($M_J \approx 0.9$), fig. 7 (a) shows that $\mathbf{S}_{\mathbf{u},s}^{(hyd,ac)}$ is localised near the nozzle lip and within the jet at an axial location around $z \approx H - D$. The region within the jet is found at the spatial location with the largest production of divergence of the velocity field (cf section 3.2). An acoustic guided jet mode (cf fig. 6) is then responsible for the closure of the feedback-loop. When the Mach number is decreased, the production of divergence of velocity is less effective and the most effective mechanism to close the feedback loop turns out to be a vortex-sound mechanism, that is, the sensitivity map $\mathbf{S}_{\mathbf{u},s}^{(hyd,ac)}$ highlights the region where the linearised Lamb vector is large (cf section 3.2). The feedback loop in this case can be closed via an acoustic pressure wave released from the region where the Lamb vector is of large magnitude and propagated as a spherical wave towards the nozzle of the lip

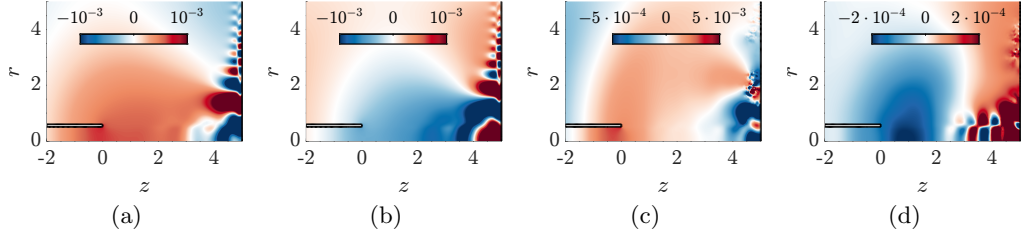


Figure 8: (a,b) Real and imaginary part of the pressure of mode (b) in fig. 3 at $M_\infty = 0.2$. (c,d) Pressure fluctuations issued from an axisymmetric time-stepping simulation at $M_\infty = 0.2$ and $Re = 2200$.

(fig. 8 (a,c)) or from inside the jet (fig. 8 (b,d)). The spatial location of the source of sound of the latter mechanism is robust with respect to modifications in the Mach or Reynolds number, i.e., the jet has a preferential location where divergence is created, and it corresponds to the region within the jet before the jet impinges the wall, cf fig. 4. On the other hand, the vortical acoustic sources along the region with a large amplitude of the linearised Lamb vector are highly sensitive to non-linear effects and to variations in the Reynolds number. The sensitivity to non-linear effects is due to the roll-up of the vortex sheet and the interaction between vortices emitted at distinct stages of the cycle. This region of the flow is dominated by vortical effects, and it becomes rapidly chaotic. From the acoustic standpoint, there exist several acoustic sources at distinct spatial positions capable to close the loop, which in turn would select a slightly different frequency of the cycle. That is, in some sense, the lack of temporal coherence of the vortical region implies a weaker frequency selection criterion. This aspect will be explored in more detail in section 5.

Figure 7 (c-d) displays the complementary sensitivity map $\mathbf{S}_{\mathbf{u},s}^{(ac,hyd)}$, which measures eigenvalue drift due to a hydrodynamic response induced by an acoustic perturbation. Not surprisingly, the impingement of acoustic perturbations onto the nozzle lip is the most effective mechanism to trigger the instability of the shear layer, which is mostly of vortical nature. Such a mechanism is largely insensitive to Mach number variations.

4.3. A finer insight to the instability core: An identification of the active flow regions

In previous sections, we have employed the structural sensitivity to identify the most sensitive regions of the flow to cause a drift to the eigenvalue (section 3.2). In addition, our refined *non-local structural sensitivity* allowed us to provide a localised stability core for a non-local instability issued from a feedback loop (section 4.2). In this section, we connect the qualitative description provided in section 3.2 in terms of physical mechanisms with a precise description of the active regions of the flow. For this purpose, we adopt the definition of the *endogeneity* proposed by Marquet & Lesshafft (2015), which yields a direct link between structural modifications in the linearised governing equations and the eigenvalue variations. The endogeneity is introduced as the scalar (complex) field measuring the eigenvalue drift when considering a localised forcing term with the same structure as the Jacobian operator $D\mathbf{F}|_{\mathbf{q}_0}$, that is, $\mathbf{H}(\hat{\mathbf{q}}) = \delta(\mathbf{x} - \mathbf{x}_0)D\mathbf{F}|_{\mathbf{q}_0}\hat{\mathbf{q}}$, which induces the following drift in the eigenvalue,

$$i\omega = \langle \hat{\mathbf{q}}^\dagger, \delta(\mathbf{x} - \mathbf{x}_0)D\mathbf{F}|_{\mathbf{q}_0}\hat{\mathbf{q}} \rangle = \langle \hat{\mathbf{q}}^\dagger(\mathbf{x}_0), D\mathbf{F}|_{\mathbf{q}_0}\hat{\mathbf{q}}(\mathbf{x}_0) \rangle \equiv E(\mathbf{x}_0) \quad (4.17)$$

with the essential property that $\int_\Omega E(\mathbf{x})d\mathbf{x} = -i\omega$. This last property is the most important feature of the endogeneity concept. The scalar field $E(\mathbf{x}_0)$ measures how local variations of the flow alter the global characteristics of the instability, such as growth

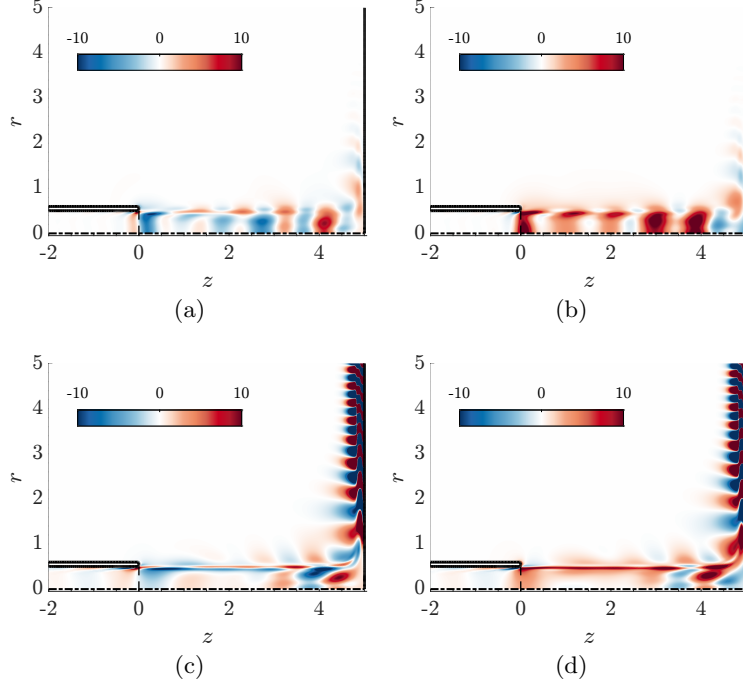


Figure 9: (a-b) Endogeneity field for mode (g) in fig. 3 at $M_\infty = 0.6$; (a) $\text{Re}(E)$, (b) $\text{Im}(E)$. (c-d) Endogeneity field for mode (b) in fig. 3 $M_\infty = 0.2$; (c) $\text{Re}(E)$, (d) $\text{Im}(E)$.

rate or frequency.

Figure 9 displays the endogeneity fields for the dominant modes at $M_\infty = 0.6$ and $M_\infty = 0.2$, respectively, which corresponds to mode (g) and mode (b) of fig. 3. The imaginary part of the endogeneity for mode (g), displayed in fig. 9 (b), is positive between the nozzle lip and the region where the module of the divergence of velocity of the mode is largest. It also corresponds to the spatial location with the largest positive real part of the endogeneity, shown in fig. 9 (a). Therefore, suggesting that the frequency is selected by the travelling time that the perturbations take to travel back-and-forth. The imaginary part endogeneity of mode (b), shown in fig. 9 (d), is composed of two regions. A region with positive sign along the axial shear layer, and another with larger magnitude and alternating sign along the radial shear layer. It suggests that the frequency is determined by the amount of the time that it takes for the perturbations to be convected downstream towards the wall, but also by the radial position of the acoustical source responsible for the pressure wave closing the feedback-loop. The real part of the endogeneity, shown in fig. 9 (a), has a similar structure to the imaginary part. The axial shear layer plays mostly a passive effect, that is, perturbations are mostly convected downstream towards the impinging wall, which has a net stabilising effect.

The endogeneity provides a further insight into the mechanisms of the instability. Since $\int_{\Omega} E(\mathbf{x}) d\mathbf{x} = -i\omega$, one can decompose the governing equations and analyse the effect that distinct mechanisms have in the instability. For this purpose, we follow a similar decomposition of the linearised compressible Navier-Stokes to the one laid out by Meliga *et al.* (2010) into production (P) and convective terms, where the latter are subdivided into advection-convection (C_A) and production-convection (C_P) terms. The

	E_{C_A}	E_{C_P}	E_P
$M_\infty = 0.6$ (g)	$-0.18 + 0.37i$	$0.49 + 1.6i$	$-0.27 + 1.4i$
$M_\infty = 0.2$ (b)	$-1.0 + 2.5i$	$1.17 + 0.79i$	$-0.14 + 0.13i$

Table 1: Decomposition of the integral of the endogeneity field, $\int_\Omega E(\mathbf{x})d\mathbf{x}$, for the dominant mode at $M_\infty = 0.6$ (g) and at $M_\infty = 0.2$ (b) in fig. 3.

decomposition is as follows,

$$\mathbf{DF}^{(C_A)}|_{\mathbf{q}_0}\hat{\mathbf{q}} \equiv \begin{cases} \mathbf{u}_0 \cdot \nabla \hat{p} + \rho_0 \nabla \cdot \hat{\mathbf{u}} \\ \hat{\rho} \mathbf{u}_0 \cdot \nabla \mathbf{u}_0 + \rho_0 \mathbf{u}_0 \cdot \nabla \hat{\mathbf{u}} \\ \rho_0 T_0 \mathbf{u}_0 \cdot \nabla \hat{s} + \hat{\rho} T_0 \mathbf{u}_0 \cdot \nabla s_0 + \rho_0 \hat{T} \mathbf{u}_0 \cdot \nabla s_0 \end{cases} \quad (4.18a)$$

$$\mathbf{DF}^{(C_P)}|_{\mathbf{q}_0}\hat{\mathbf{q}} \equiv \begin{cases} \hat{\rho} \nabla \cdot \mathbf{u}_0 + \hat{\mathbf{u}} \cdot \nabla \rho_0 \\ \rho_0 \hat{\mathbf{u}} \cdot \nabla \mathbf{u}_0 \\ \rho_0 T_0 \hat{\mathbf{u}} \cdot \nabla s_0 \end{cases} \quad (4.18b)$$

$$\mathbf{DF}^{(P)}|_{\mathbf{q}_0}\hat{\mathbf{q}} \equiv \begin{cases} 0 \\ \nabla \hat{p} - \frac{1}{Re} \nabla \cdot \tau(\hat{\mathbf{u}}) \\ -\gamma(\gamma-1) \frac{M_\infty^2}{Re} (\tau(\hat{\mathbf{u}}) : \mathbf{D}(\mathbf{u}_0) + \tau(\mathbf{u}_0) : \mathbf{D}(\hat{\mathbf{u}})) - \frac{\gamma}{Pr Re} \Delta \hat{T} \end{cases} \quad (4.18c)$$

And we define the endogeneity fields for each of the operators,

$$E^{C_A}(\mathbf{x}) \equiv \hat{\mathbf{q}}^\dagger(\mathbf{x}) \cdot \mathbf{DF}^{C_A}|_{\mathbf{q}_0}\hat{\mathbf{q}}(\mathbf{x}) \quad (4.19a)$$

$$E^{C_P}(\mathbf{x}) \equiv \hat{\mathbf{q}}^\dagger(\mathbf{x}) \cdot \mathbf{DF}^{C_P}|_{\mathbf{q}_0}\hat{\mathbf{q}}(\mathbf{x}) \quad (4.19b)$$

$$E^P(\mathbf{x}) \equiv \hat{\mathbf{q}}^\dagger(\mathbf{x}) \cdot \mathbf{DF}^{(P)}|_{\mathbf{q}_0}\hat{\mathbf{q}}(\mathbf{x}) \quad (4.19c)$$

Table 1 reports the global contribution to the instability of the three operators defined in eq. (4.18). For the two modes, the convection-advection and production operators have a global stabilising effect, whereas the convection-production operator plays a global destabilising role. Their spatial distributions (real part) are shown in fig. 10. The convection-production term provides the main root of the growth rate. The largest contribution coming from the base flow shear $\rho_0 \hat{\mathbf{u}} \cdot \nabla \mathbf{u}_0$ term, which is active along the axial shear layer, see fig. 10 (b,e). The convection-advection operator is globally stabilising, however it plays an active role in advecting the perturbation to the instability core. Visual inspection of the real part of the E^{C_A} field, displayed in fig. 10 (a,d), suggests that at large Mach numbers the acoustic perturbations are propagated along the shear layer to the region of largest divergence of the fluctuating velocity field. On the other hand, at low Mach number, the downstream convection of perturbation counteracts the local growth and makes the instability more convective. Concerning the production terms, at large Mach number, the field, displayed in fig. 10 (c), is positive inside the jet from the nozzle lip to $z \approx H - D$. The effect on the growth rate seems to be associated to the backward propagation of the guided jet mode from the region around $z \approx H - D$ to the nozzle-lip. Instead, at low Mach numbers, the dominant production term is the pressure gradient, which enforces the continuity condition by inducing a perturbation of the volume flux across the shear layer, cf Marquet & Lesshafft (2015). In the region

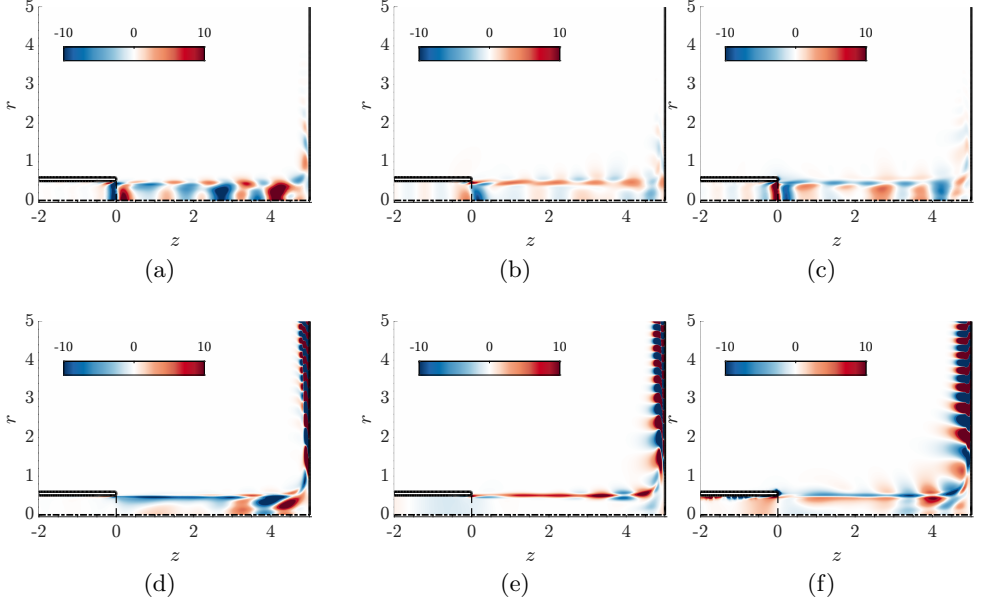


Figure 10: (a-c) Endogeneity field for mode (g) in fig. 3 at $M_\infty = 0.6$; (a) E^{C_A} , (b) E^{C_P} , (c) E^P . (e-f) Endogeneity field for mode (b) in fig. 3 $M_\infty = 0.2$; (d) E^{C_A} , (e) E^{C_P} , (f) E^P .

between the nozzle lip and the impinging wall counteracts the effect of the advection operator inside the jet, and it favours the convective effect outside the jet.

Finally, motivated by the significant role played by the divergence of the velocity perturbations in the closure of the feedback-loop at large Mach number, we analyse the effect on the growth rate of local modifications of the divergence of the momentum equation (eq. (3.1)). To do so, we take the inner product of the acoustic velocity adjoint $\hat{\mathbf{u}}_{ac}^\dagger$ with the momentum equation, which by integration by parts leads to the following definition of E_{div} ,

$$\begin{aligned} i\delta\omega_{\text{div}} &= \langle -\nabla\phi^\dagger, \delta(\mathbf{x} - \mathbf{x}_0)D\mathbf{F}_{(\text{mom})}|_{\mathbf{q}_0}\hat{\mathbf{q}} \rangle \\ &= \langle \phi^\dagger, \delta(\mathbf{x} - \mathbf{x}_0)\nabla \cdot D\mathbf{F}_{(\text{mom})}|_{\mathbf{q}_0}\hat{\mathbf{q}} \rangle + \text{B.T.} \end{aligned} \quad (4.20a)$$

$$E_{\text{div}} \equiv \phi^\dagger(\mathbf{x})(\nabla \cdot D\mathbf{F}_{(\text{mom})}|_{\mathbf{q}_0}\hat{\mathbf{q}})(\mathbf{x}), \quad (4.20b)$$

where it can be shown that the boundary terms (B.T.) are null in the impinging jet configuration. Following the same approach as in eq. (4.19), we can split we split $E_{(\text{div})}$ and analyse the effect of the three aforementioned operators on the growth rate. Such analysis renders possible to study the effect on the growth rate of the physical mechanisms generating and advecting the divergence of the velocity field. Figure 11 (a) displays the real part of the $E_{(\text{div})}$. Not surprisingly, the largest positive contribution comes from the region with the largest divergence of the mode ($z \approx H - D$). The convection production term, displayed in fig. 11 (c), peaks in the region of largest divergence of the baseflow, which suggests a local conversion of divergence from the baseflow to the perturbations. The structure of the convection-advection and production terms is more intriguing. The $E_{\text{div}}^{C_A}$ and E_{div}^P are almost identical, but of opposite sign, suggesting that the role of the pressure is to counteract the advection of fluctuating divergence. The shear layer, delimits

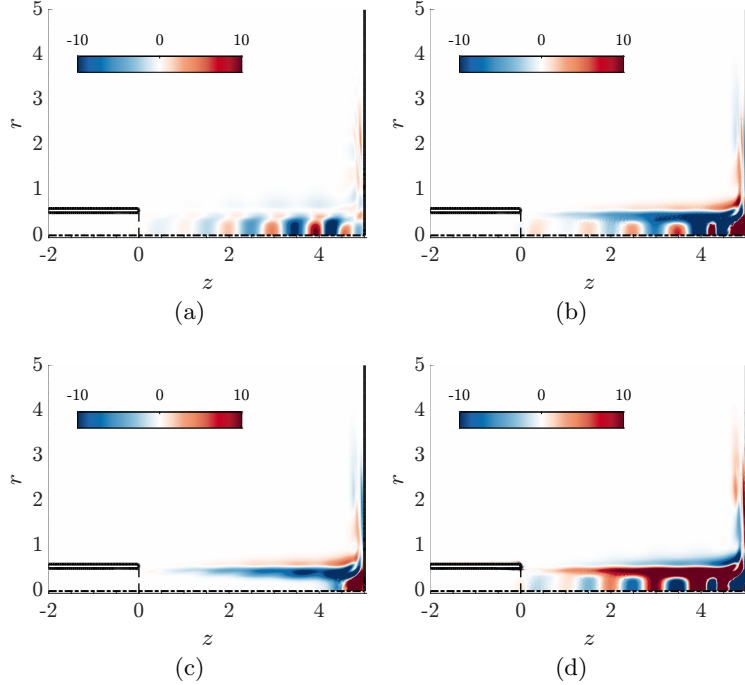


Figure 11: (a) Endogeneity field of the divergence of the momentum equation E_{div} . (b) E_{div}^{CA} . (c) E_{div}^{CP} . (d) E_{div}^P .

the region inside and outside the jet. Inside the jet, the production of divergence of the fluctuating velocity field has a destabilising effect; instead, the advection of divergence inside the jet renders the instability more convective. The largest growth rate drift by the production of a divergence is observed to happen along thin radial layers inside the jet. The spatial distribution of E_{div}^P composed of cell structures vaguely resembles the shock-cell structure observed in supersonic jets (Edgington-Mitchell *et al.* 2018), where the divergence of the velocity field is produced across the shock cell. Thus, suggesting a connection between the production of divergence and the instability mechanisms between large subsonic and supersonic Mach numbers.

4.4. Wave decomposition of the feedback mechanism

Herein, we perform a weakly non-parallel local decomposition of the different waves supported by the base flow. The configuration under investigation contains in fact an extended region of quasi-parallel flow, where a simplified analysis can be used to investigate the local stability property of the jet and the supported waves. Specifically, in regions where the flow is almost parallel, we perform a multiple-scale analysis: the disturbance is assumed to have the following asymptotic expansion

$$\mathbf{q}(r, Z) = e^{-i\phi(Z)/\varepsilon} \sum_{n,k} C_k(Z) \mathbf{q}_{n,k}^{(\varepsilon)}(r, Z) \varepsilon^n , \quad (4.21)$$

where the slow variable $Z = \varepsilon z$ is kept $O(1)$ in the limit $\varepsilon \rightarrow 0$. Here the expansion parameter ε is defined as the ratio of the two main length scales occurring in the problem, i.e $\varepsilon = \frac{\ell_W^*}{\ell_B^*}$ where ℓ_B^* is the characteristic scale over which the base flow experiences an $O(1)$ variation, while ℓ_W^* is the characteristic wavelength of the perturbation. Note that

the expansion (4.21) depends on both ε and $\epsilon = 1/Re$ owing to the base flow dependence on the Reynolds number. For our purpose it is not necessary to provide an explicit relation between the two parameters, but it suffices to assume $\varepsilon \sim O(1/Re)$. The validity of the previous assumptions can be verified a posteriori.

In eq. (4.21) we consider the primitive variables $\hat{\mathbf{q}} = [\hat{p}, \hat{\mathbf{u}}, \hat{p}, \hat{T}]$, that is, the vector containing the components of the disturbance field. The phase $\phi = -\int(\alpha(Z) + \delta\alpha(Z))dZ$ is a slowly-varying function of Z to be determined during the asymptotic procedure. The slow varying amplitude $C_k(Z)$ should be interpreted as the projection of the global mode onto the local waves supported by the baseflow, and it is also determined using the asymptotic procedure. Introducing eq. (4.21) into the linearised system, up to $O(\varepsilon)$, and collecting different powers of ε , we are left with the following series of problems describing the evolution of the perturbation,

$O(\varepsilon^0)$

$$(-i\omega\mathbf{B}|_{\mathbf{q}_0} + \mathbf{DF}(\alpha)|_{\mathbf{q}_0})\mathbf{q}_{0,k}^{(\varepsilon)}(r, Z) = \mathbf{0} \quad (4.22a)$$

$$u_0, v_0, p_0 \rightarrow 0 \quad \text{as } r \rightarrow \infty \quad (4.22b)$$

$$u_0 = v_0 = 0 \quad \text{at } r = 0 \quad (4.22c)$$

$O(\varepsilon^1)$

$$(-i\omega\mathbf{B} + D\mathbf{F}(\alpha))\mathbf{q}_{1,k}^{(\varepsilon)}(r, Z) = i\frac{d}{d\alpha}(-i\omega\mathbf{B} + D\mathbf{F}(\alpha))\frac{d\mathbf{q}_{0,k}^{(\varepsilon)}}{dZ} \quad (4.23a)$$

$$u_1, v_1, p_1 \rightarrow 0 \quad \text{as } r \rightarrow \infty \quad (4.23b)$$

$$u_1 = v_1 = 0 \quad \text{at } r = 0. \quad (4.23c)$$

At $O(\varepsilon^0)$ the problem is linear, and we determine the pair $(\alpha(Z), \mathbf{q}_{0,k}^{(\varepsilon)}(r, Z))$ from the resolution of the eigenvalue problem eq. (4.22). At the next order, $O(\varepsilon^1)$, the problem has a forcing secular term, which needs to be removed by imposing the solvability condition. The solvability condition provides the weakly-non-parallel correction of the phase, herein named $\delta\alpha(Z)$, and defined as

$$\delta\alpha = \frac{\mathbf{q}_{0,k}^{\dagger,(\varepsilon)} \cdot \left[\frac{d}{d\alpha}(-i\omega\mathbf{B} + D\mathbf{F}(\alpha)) \frac{d\mathbf{q}_{0,k}^{(\varepsilon)}}{dZ} \right]}{\mathbf{q}_{0,k}^{\dagger,(\varepsilon)} \cdot \left[\frac{d}{d\alpha}(-i\omega\mathbf{B} + D\mathbf{F}(\alpha)) \mathbf{q}_{0,k}^{(\varepsilon)} \right]}. \quad (4.24)$$

In the previous expression, $\mathbf{q}_{0,k}^{\dagger,(\varepsilon)}$ is the adjoint solution of the linear problem eq. (4.22). Finally, we determine the projection of the global mode onto the k^{th} local wave. We use the local adjoint solution of the k^{th} wave to determine the slowly varying amplitude,

$$C_k(Z) = \mathbf{q}_{0,k}^{\dagger,(\varepsilon)} \cdot \left[\frac{d}{d\alpha}(-i\omega\mathbf{B} + D\mathbf{F}(\alpha)) \hat{\mathbf{q}}(r, z) \right] e^{-i \int \alpha_k + \delta\alpha_k dZ}, \quad (4.25)$$

with $\hat{\mathbf{q}}(r, z)$ the global mode.

Figure 12 (a) displays the spectrum of the linear spatial stability problem eq. (4.22) for a baseflow at $Re = 800$ and $M_\infty = 0.6$ (Mode (g) in fig. 3) at the mid-point between the nozzle lip and the impinging wall ($z = 2.5D$). The spectrum displays a set of modes along the axis, which belong to the continuous branches α^+ and α^- of free-stream acoustic modes (Towne *et al.* 2017). Another set of modes emerge from the right end of the spectrum for $\text{Im}(\alpha) > 0$, these modes approximate the entropy continuous branch. There are also four discrete modes. Two duct modes, named D^\pm with the upper script indicating the direction of propagation. The radial support of these two modes lies inside the jet.

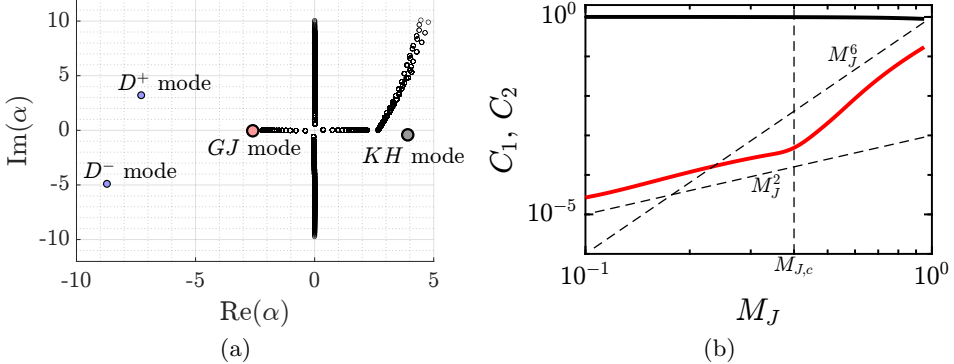


Figure 12: (a) Spectrum of the linear spatial stability problem eq. (4.22) for a baseflow at $Re = 800$ and $M_\infty = 0.6$ (Mode (g) in fig. 3) at the mid-point between the nozzle lip and the impinging wall ($z = 2.5D$). (b) Evolution of the projection coefficients C_1 (Kelvin-Helmholtz mode) and C_2 (Guided-Jet mode) with respect to the Mach number of the jet (M_J).

There is a guided jet mode, which is found at the left of the free-stream continuous branch, that is, it possesses a slower phase speed than the free-stream sound speed. The radial support inside the jet of the pressure component is similar to the duct modes, but it also possesses a radial support outside the jet. There is also a Kelvin-Helmholtz or shear layer mode, with a radial support around the shear layer of the baseflow.

The projection coefficient (C_k) of the global mode onto the duct modes is nearly null. Hereafter, we consider that the global mode is composed only of the shear layer mode (mode 1) and the guided jet wave mode (mode 2), that is, we truncate the sum in eq. (4.21) to just two modes. The global mode and the local waves are normalised with the energy of the fluctuations (Chu 1965). From this assumption, at neutrality, one can recover the reflection coefficient by considering the ratio between the two waves, here we define the reflection coefficient as $r = \frac{C_2(Z_m)}{C_1(Z_m)}$, with $Z_m = H/2$ the mid-point between the impinging wall and the nozzle lip. In the central region, the two slowly varying amplitudes are nearly constant (not shown), which justifies its usage to determine the local properties of the waves. Figure 12 (b) shows the evolution of the two projection coefficients of the local waves onto the global mode. The coefficient of the shear layer mode C_1 is nearly constant and equal to unity. Thus, the evolution of C_2 with respect to the Mach number of the jet provides a direct characterisation of the reflection coefficient. The coefficient of the guided jet mode is $O(10^{-1})$ at large Mach numbers, it evolves roughly as M_J^6 in the interval $(M_{J,c}, 0.9)$, and then it decreases as M_J^2 in the interval $(0, M_{J,c})$, with $M_{J,c} \approx 0.4$. The transition in the reflection coefficient dependency with the Mach number of the jet is another consequence of the modification of the instability mechanism, from the closure of the feedback loop by propagation of the divergence of velocity created within the jet to the closure of the loop by vortical acoustic sources outside the jet near the wall.

5. Nonlinear dynamics of the impinging jet

Herein, we study the dynamics of the normal form involving three global modes, which is the simplest equation displaying tonal dynamics, that is periodic or quasiperiodic resonant solutions, and the decoupling of the resonant mode. We also compare the

numerical results obtained from axisymmetric time-stepping simulations at different M_∞ for fixed $Re = 2000$. In addition, we propose a phenomenological model to account for the transition to broadband dynamics using a simple model of additive Gaussian noise on the resonant phase.

5.1. Normal form reduction – Analysis

First, we express eq. (B 20) of section 2.4 in the polar coordinates of the complex amplitudes $z_k(\tau) = r_k(\tau)e^{i\phi_k(\tau)}$. This procedure allow us to reduce the dimension of the normal form from six (three complex amplitudes) to four, three equations for the real amplitudes and an equation for a resonant phase $\psi = (\phi_3 - \phi_2) - (\phi_2 - \phi_1)$,

$$\begin{aligned}\dot{r}_1 &= r_1 [\lambda_1^R + \nu_{11}^R r_1^2 + \nu_{12}^R r_2^2 + \nu_{13}^R r_3^2] + r_2^2 r_3 [\cos(\psi) \chi_1^R + \sin(\psi) \chi_1^I] \\ \dot{r}_2 &= r_2 [\lambda_2^R + \nu_{21}^R r_1^2 + \nu_{22}^R r_2^2 + \nu_{23}^R r_3^2] + r_1 r_2 r_3 [\cos(\psi) \chi_2^R - \sin(\psi) \chi_2^I] \\ \dot{r}_3 &= r_3 [\lambda_3^R + \nu_{31}^R r_1^2 + \nu_{32}^R r_2^2 + \nu_{33}^R r_3^2] + r_2^2 r_1 [\cos(\psi) \chi_3^R + \sin(\psi) \chi_3^I] \\ \dot{\psi} &= \delta\omega + \cos(\psi) [-\chi_3^I r_1 r_2^2 / r_3 + 2\chi_2^I r_1 r_3 - \chi_1^I r_3 r_2^2 / r_1] \\ &\quad - \sin(\psi) [\chi_3^R r_1 r_2^2 / r_3 + 2\chi_2^R r_1 r_3 + \chi_1^R r_2^2 r_3 / r_1].\end{aligned}\quad (5.1)$$

Here, we use the notation $\delta\omega \equiv \delta\omega^L + \delta\omega^{NL}$ with $\delta\omega^L \equiv [\omega_1 + \omega_3 - 2\omega_2]$ the linear frequency mismatch at criticality, and the nonlinear frequency mismatch $\delta\omega^{NL} = \Delta\omega_2^{NL} - \Delta\omega_1^{NL} = [\omega_1^{NL} + \omega_3^{NL} - 2\omega_2^{NL}]$, where $\omega_k^{NL} = \lambda_k^I + \nu_{k1}^I r_1^2 + \nu_{k2}^I r_2^2 + \nu_{k3}^I r_3^2$ for $k = 1, 2, 3$. The upper scripts R and I are used to denote the real and imaginary part of the coefficient.

We analyse the solutions of eq. (5.1) in two steps, first we summarise the results of the non-resonant case ($\chi_1 = \chi_2 = \chi_3 = 0$), which was studied more in detail for the case of the mode interaction in the wake flow behind a rotating sphere (Sierra-Ausín *et al.* 2022). Subsequently, we discuss, in the presence of resonant coupling, the phase-locked transition from a resonant quasiperiodic state to a modulated three frequency state with a small frequency modulation. The new modulating frequency, being proportional to the imperfections in the frequency quantization ($\delta\omega^{NL}$), is expected to induce a transition to a chaotic attractor, following the route to chaos suggested by Ruelle–Takens–Newhouse, when this new frequency is of the order of the frequency difference between two modes, e.g., $\Delta\omega_1^{NL}$.

5.1.1. Stochastic modelling

Ruelle–Takens–Newhouse (Newhouse *et al.* 1978) state that one may obtain a chaotic Axiom A attractor by perturbing a three-tori solution, with a given arbitrarily small perturbation. However, it fails to provide the precise route to chaos, which may occur following a torus breakdown (Tanaka 2005), which occurs because of the loss of smoothness of the two or three tori attractors (Marques *et al.* 2001). In order to account for the loss of smoothness of the system, we replace

$$\delta\omega^{NL} \mapsto \delta\omega^{NL}(1 + dW),$$

with dW a differential Wiener process and $\delta\omega^{NL}$ determined from the deterministic normal form. This phenomenological modelling is based on the fact that the sources of sound responsible for the closure of the feedback become less coherent with decreasing Mach number (see section 4). Such a modelling is faithful with the deterministic normal form eq. (5.1) in the mean sense, that is, $\mathbb{E}(\delta\omega^{NL}(1 + dW)) = \delta\omega^{NL}$. At low subsonic Mach number, the increase of $\delta\omega^{NL}$ is caused by the elongated nature of the wavemaker, which enables the existence of sources of vortex sound at distinct spatial locations. Each

Name	Representative Frequencies
TS (Trivial state)	(0, 0, 0, n.d.)
PW (Periodic Wave mode)	(r_a , 0, 0, n.d.)
MW (Mixed Wave mode)	(r_a , r_b , 0, n.d.)
3FW (Three Frequency Wave mode)	(r_a , r_b , r_c , n.d.)
MrW (Mixed resonant Wave mode)	(r_a , r_b , r_c , ψ_d)

Table 2: Nomenclature of fixed point solutions of the system eq. (5.1). The MW and the 3FW correspond to the case of non-resonant coupling $\chi_1 = \chi_2 = \chi_3 = 0$.

of these sources it is associated with a distinct fundamental frequency $\Delta\omega$, which is inversely proportional to the convective time it takes for the hydrodynamic perturbations to reach the source of vortex sound at the wavemaker and to the acoustic time it takes for the perturbation to reach back to the lip of the nozzle. Therefore, providing a phenomenological interpretation to the increase of the modulation frequency with a decreasing Mach number. Thus, the transition to a broadband spectrum can be interpreted as the consequence of the loss of coherence of the feedback process and the fact that the levels of the sound acoustic pressure decrease with decreasing Mach number. The latter effect is attributed to the fact that with decreasing Mach number, the production of the divergence of velocity field is reduced, which occurs mostly within the jet and near the wall. Additionally, the propagation of the guided jet wave becomes less effective with decreasing Mach number, because of the increase of its wavelength. This phenomenon can be appreciated in fig. 7, where the structural sensitivity to the acoustic response of the system from hydrodynamic perturbations is displaced from a spatial location within the jet to an elongated region near the wall outside the jet.

5.1.2. Properties of the deterministic normal form

In the absence of a coupling between the real amplitudes r_k and the resonant phase ψ , i.e. $\chi_1 = \chi_2 = \chi_3 = 0$, we have that $\psi = (\omega_2^{NL} - \omega_1^{NL})t - (\omega_3^{NL} - \omega_2^{NL})t$, which is generally non-zero. In this case, eq. (5.1) is simplified to

$$\begin{aligned}\dot{r}_\ell &= r_\ell \left[\Lambda_\ell^R + \mathcal{V}_{\ell k}^R r_k^2 \right], \quad k, \ell = 1, 2, 3, \\ \dot{\phi}_\ell &= \Lambda_\ell^I + \mathcal{V}_{\ell k}^I r_k^2, \quad k, \ell = 1, 2, 3,\end{aligned}\tag{5.2}$$

where $\Lambda = \Lambda^R + \Lambda^I \equiv (\lambda_1, \lambda_2, \lambda_3)^T$ and the matrix $\mathcal{V} = \mathcal{V}^R + i\mathcal{V}^I$ is

$$\mathcal{V} \equiv \begin{pmatrix} \nu_{11} & \nu_{12} & \nu_{13} \\ \nu_{21} & \nu_{22} & \nu_{23} \\ \nu_{31} & \nu_{32} & \nu_{33} \end{pmatrix}\tag{5.3}$$

To ease the presentation of the fixed point solutions of eq. (5.2), let us introduce the inverse of the linear operator \mathcal{V} , which can be written as

$$\mathcal{V}^{-1} = \frac{1}{\det \mathcal{V}} \begin{pmatrix} \det \mathcal{V}_{11} & \det \mathcal{V}_{21} & \det \mathcal{V}_{31} \\ \det \mathcal{V}_{12} & \det \mathcal{V}_{22} & \det \mathcal{V}_{32} \\ \det \mathcal{V}_{13} & \det \mathcal{V}_{23} & \det \mathcal{V}_{33} \end{pmatrix},\tag{5.4}$$

where $\det \mathcal{V}_{k\ell}$ denotes the minor of the matrix \mathcal{V} , obtained by eliminating the line k and the column ℓ .

This equation has four types of solutions, listed in table 2 with their respective nomenclature and number of independent frequencies. The definition of the solutions

Name of solutions	Definition	Eigenvalues
PW_i (for $i = 1, 2, 3$)	$r_i^{(PW)} = \sqrt{-\frac{\lambda_i^R}{\nu_{ii}^R}}$	$-\lambda_i^R,$ $\lambda_j^R - \nu_{ji}^R \frac{\lambda_i^R}{\nu_{ii}^R}, \text{ for } j \neq i$
$MW_{ij}, (i, j = 1, 2, 3)$ $(j \neq i, k \neq i, k \neq j)$	$r_i^{(MW_{ij})} = \sqrt{\frac{\lambda_j^R \nu_{ij}^R - \lambda_i^R \nu_{jj}^R}{\det(\mathcal{V}_{kk})}}$ $r_j^{(MW_{ij})} = \sqrt{\frac{\lambda_i^R \nu_{ji}^R - \lambda_j^R \nu_{ii}^R}{\det(\mathcal{V}_{kk})}}$	$\frac{\nu_{ii}^R r_i^2 + \nu_{jj}^R r_j^2}{2} \pm \sqrt{(\nu_{ii}^R r_i^2 - \nu_{jj}^R r_j^2)^2 / 4 + \nu_{ij}^R \nu_{ji}^R r_i^2 r_j^2}$ $\frac{1}{\det(\mathcal{V}_{kk}^R)} [\lambda_k^R \det(\mathcal{V}_{kk}^R) + \lambda_i^R \det(\mathcal{V}_{ik}^R) + \lambda_j^R \det(\mathcal{V}_{jk}^R)]$
$3FW_{123}$	$(r_1^2, r_2^2, r_3^2)^T = -(\mathcal{V}^R)^{-1} \Lambda^R$	Eigs of $D\mathbf{f}^R$

Table 3: Defining equations and eigenvalues of the solutions of the polar third order normal form eq. (5.1) in the case of non-resonant coupling $\chi_1 = \chi_2 = \chi_3 = 0$. $D\mathbf{f}^R$ denotes the Jacobian matrix of the polar amplitudes of eq. (5.2).

and their linear stability is enumerated in table 3. The two solutions of interest for us are the PW and the MW, which are representative of *tonal* dynamics.

Now, we turn our attention to the resonant case. In particular, we focus on the dynamics of a resonant MW state, which is a quasiperiodic state and the amplitudes r_1 and r_2 determined as in table 3, with a constant resonant amplitude r_3 and locked phase ψ . This new state, referred to as Mixed resonant Wave (MrW) still possesses two incommensurate frequencies, with the third mode resonant to the other two. A definition of this resonant solution may be found in table 4. The MrW branch may display a Hopf bifurcation, which, in the case of $r_3 \ll r_1, r_2$, can be analysed by simply studying the two-by-two sub-block of the Jacobian matrix of eq. (5.1). The MrW_{12} branch loses stability in a Hopf bifurcation with a modulation frequency $\omega' \propto \delta\omega^{NL}$, see the last column of table 4. It occurs when the attracting eigenvalue in the r_3 -direction is smaller than $-\sigma_{MW_{12}} \leq \frac{\chi_3^I}{\chi_3^R} \delta\omega$. The right-hand side of the inequality can be interpreted as the effective frequency mismatch $\delta\omega^{\text{eff}} \equiv \frac{\chi_3^I}{\chi_3^R} \delta\omega$ induced by the coupling coefficients. The Modulated Mixed drift Wave (MMdW) is susceptible to be observed as a chaotic attractor when studying the Navier–Stokes equations. However, it is possible to observe this new three-frequency state as a non-chaotic attractor when the modulation frequency is much smaller than the other two frequencies $\omega' \ll \omega_1, \omega_2$, which occurs if $\delta\omega \ll 1$. Similarly, in the actual dynamics of the Navier–Stokes equation, a chaotic attractor is likely to shadow the MMdW state, which is expected to occur when the third amplitude (r_3) is sufficiently large. Therefore, in this sense, we cannot provide a sharp cut-off for the transition of broadband (chaotic) - tonal dynamics, but we provide a qualitative description of the transition in the simplest case with resonance between the modes of the spectrum. In the following sections, we provide a comparison of the deterministic and stochastic normal forms with direct numerical simulations of the axisymmetric impinging jet.

Name of solutions	Definition	Stability
MrW ₁₂	$\tan(\psi) = -\frac{\chi_3^R \delta\omega + \sigma_{MW_{12}} \chi_3^I}{\chi_3^I \delta\omega + \sigma_{MW_{12}} \chi_3^R}$ $r_3 = \frac{(\chi_3^R)^2 - (\chi_3^I)^2}{\chi_3^R \delta\omega + \sigma_{MW_{12}} \chi_3^I} r_2^2 r_1 \sin(\psi)$	$\frac{2\chi_3^R (\delta\omega \chi_3^I + \chi_3^R \sigma_{MW_{12}})}{(\chi_3^R)^2 - (\chi_3^I)^2} > 0$ $\omega' = \left \frac{\delta\omega}{\chi_3^R} \left((\chi_3^R)^2 - (\chi_3^I)^2 \right)^{1/2} \right $

Table 4: Defining equations and eigenvalues of the Mixed resonant wave of eq. (5.1) in the case of resonant coupling. The amplitudes r_1 and r_2 are defined in table 3, since they are the same as for the MW_{12} . The eigenvalue $\sigma_{MW_{12}} = \frac{1}{\det(\mathcal{V}_{33}^R)} \left[\lambda_3^R \det(\mathcal{V}_{33}^R) + \lambda_1^R \det(\mathcal{V}_{13}^R) + \lambda_2^R \det(\mathcal{V}_{23}^R) \right]$ is the eigenvalue of the MW in the direction of r_3 . ω' is defined criticality, that is, when $\sigma_{MW_{12}} = \frac{\chi_3^I}{\chi_3^R} \delta\omega$.

5.2. Results

5.2.1. Small subsonic Mach number – An example of broadband noise

At low Mach numbers, a broadband spectrum characterizes the dynamical attractor (obtained from axisymmetric numerical simulations, section 2.3), which is displayed in fig. 13 (b) with red, blue and black solid lines for pressure probes at an axial location $z = 0$ and a radial position $r = 1D$, $r = 2D$ and $r = 4D$, respectively. This type of dynamics is *modelled* by a periodic solution (MMdM) of the normal form eq. (5.1), which is a three-tori solution in the original coordinates of the ansatz eq. (2.11). The MMdM solution emerges almost directly from the PW₂ branch (fig. 13 (a)), that is, the MrW₁₃ is unstable (not shown). The Modulated Mixed drift Wave possesses a modulation frequency $\omega' \approx \Delta\omega$, that is, the modulation frequency has a similar magnitude to the frequency difference between the other two dominant frequencies. In that scenario, the original dynamics of the Navier–Stokes equations are expected to be chaotic with a broadband spectrum. However, fig. 13 shows a tonal spectrum (yellow line), which has been obtained from the deterministic normal form. Such a feature is characteristic of this particular type of normal form, and it is a pathological property of the truncation. Instead, when considering the stochastic model with $\delta\omega \approx 0.1$, one obtains a spectrum (green line) which offers a considerably better comparison with respect to the data of the axisymmetric simulation. In this case, the spectrum displays a wide peak of small magnitude around f_1 and f_2 , and a broadband spectrum with a similar slope to the numerical results (red line). Thought the matching is not perfect, the ratio between the peak and the broadband levels is slightly larger in the deterministic model, which suggests a higher degree of stochasticity of the axisymmetric numerical simulation. The difference may be explained from the fact that the axisymmetric numerical simulations allow for a vortical feedback, vortices emitted by the roll-up of the radial shear layer near the wall and outside the jet are propagated towards the lip. These vortices are produced aperiodically in a chaotic region of the flow, thus reducing the coherence of the spectrum when they induce a hydrodynamic instability near the lip of the nozzle. Such a feature is strongly nonlinear, and it is not accounted by the normal form. A possible correction to the stochastic model would consist in the inclusion of a diffusion coefficient $\sqrt{D_{\text{eff}}}$ in $\delta\omega(1 + \sqrt{D_{\text{eff}}} dW)$, and thus determine the effective diffusion from the fitting of numerical or experimental data (Callaham *et al.* 2021).

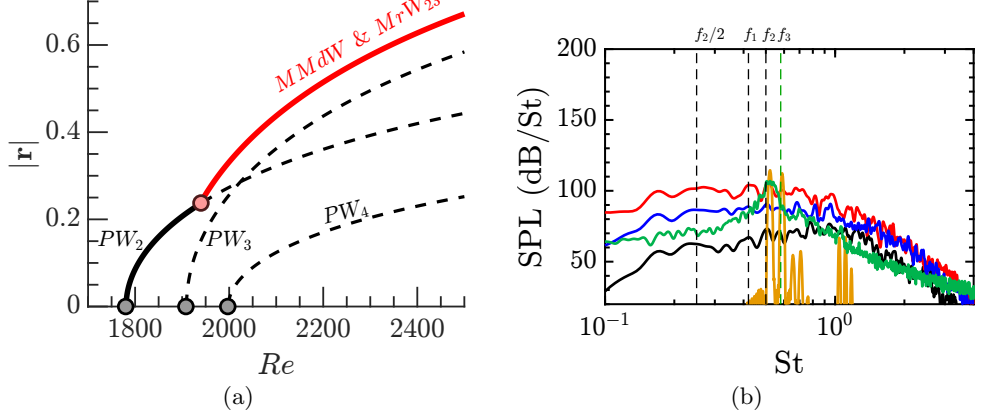


Figure 13: (a) Bifurcation diagram at $M_\infty = 0.3$ with respect to the Reynolds number with $|\mathbf{r}| = \sqrt{r_1^2 + r_2^2 + r_3^2}$. Solid lines indicate stable attractors, dashed lines indicate unstable fixed points of eq. (5.1). (b) Sound pressure levels at $Re = 2000$. Probes of instantaneous pressure fluctuations at the axial location $z = 0$ and radial positions $r = 1D$ (red - axisymmetric time-stepping, yellow - deterministic normal form, green stochastic normal form with $\delta\omega = 0.1$), $r = 2D$ (black - axisymmetric time-stepping) and $r = 4D$ (dark blue - axisymmetric time-stepping). The vertical dashed lines highlight the frequencies of the peaks obtained with the axisymmetric time-stepping simulation.

5.2.2. Large subsonic Mach number – An example of weakly resonant tones

At large Mach numbers, the dynamical attractor is characterized by a tonal spectrum with large peaks at discrete frequencies. This type of dynamics is *modelled* by a fixed-point (MrW) or a periodic solution (MMdW) of the normal form eq. (5.1). Figure 14 (a) shows the bifurcation diagram obtained with the deterministic normal form. The mode-switching point reported in section 3 was located at $M_\infty^A \approx 0.49$. For larger values of M_∞ the PW_3 branch emerges from the primary bifurcation as a stable solution, and the PW_2 branch subsequently bifurcates. The PW_2 branch is unstable near the onset of instability, and it is restabilised following a subcritical bifurcation of the MrW_{23} branch. Figure 14 (a) shows the existence of regions with multiple stable attractors (PW_2 and PW_3 , and MW_{13} and $MMdW$), a feature that was also observed in the experimental campaign of Nosseir & Ho (1982) at large Mach numbers of the jet. Specifically, the $MMdW$ coexists with a stable non-resonant quasiperiodic solution (MW_{13}). The MW_{13} state becomes unstable via a symmetry breaking bifurcation to a MrW_{13} . The MrW_{13} branch experiences a saddle-node bifurcation and it folds onto itself to finally reconnect to the MW_{13} branch again. Because of the saddle-node bifurcation in the MrW_{13} branch, after the second re-connection, the MW_{13} branch continues to be unstable. In addition, even when the MW_{13} branch is stable, its basin of attraction is considerably smaller than the one of the $MMdW$ state, and it shrinks with increasing Reynolds number. That is, in the interval of coexistence of the two branches, most of initial conditions are attracted to the $MMdW$ state. In the following, we simply consider the case at $Re = 2000$ of the $MMdW$ state. In this case, the modulation frequency of the Modulated Mixed resonant Wave is smaller than the frequency difference between the modes ($\omega' \ll \Delta\omega$). In that scenario, the spectrum of the Navier-Stokes equations is expected to be weakly tonal with wide and large magnitude peaks. In this case, the deterministic normal form offers a good qualitative description of the spectrum, it is able to identify the main

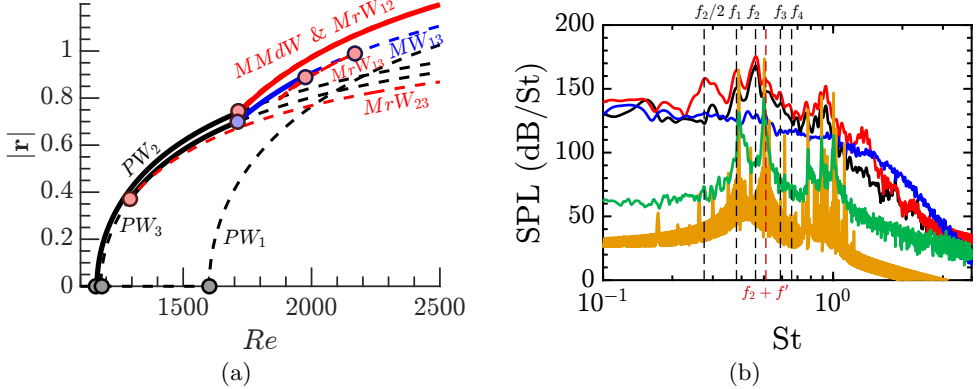


Figure 14: (a) Bifurcation diagram at $M_\infty = 0.5$ with respect to the Reynolds number with $|r| = \sqrt{r_1^2 + r_2^2 + r_3^2}$. Solid lines indicate stable attractors, dashed lines indicate unstable fixed points of eq. (5.1). (b) Sound pressure levels at $Re = 2000$. Probes of instantaneous pressure fluctuations at the axial location $z = 0$ and radial positions $r = 1D$ (red - axisymmetric time-stepping, yellow - deterministic normal form, green stochastic normal form with $\delta\omega \approx 0.04$), $r = 2D$ (black - axisymmetric time-stepping) and $r = 4D$ (dark blue - axisymmetric time-stepping). The vertical dashed lines highlight the frequencies of the peaks obtained with the axisymmetric time-stepping simulation.

frequency peaks and the frequency modulation f' . The frequency modulation obtained from numerical simulations is $f'_{DNS} \approx 0.05$, while the frequency modulation from the normal form is $f' \approx 0.04$. Additionally, as in the broadband case, we compare in fig. 14 the results of the axisymmetric numerical simulation (red line) with those of the deterministic normal form (yellow line) and the stochastic model (green line). It shows a reasonable comparison, though the sound pressure levels are underestimated, between the spectrum of the Navier–Stokes equations and the one from the stochastic model. However, since the model is weakly nonlinear, it fails to predict the existence of a peak at $f_2/2$, which occurs because of a secondary instability of the radial shear layer. Inspection of the numerical results suggests that such a frequency peak occurs because of a vortex-pairing instability of the radial shear layer (Shaabani-Ardali *et al.* 2019).

6. Discussion & Conclusion

The dynamics of the hydrodynamic-acoustic feedback instability of a rounded laminar subsonic impinging jet configuration has been analysed. First, it has been shown the existence for every Mach number of a family of unstable modes, which are characterised by their axial wavenumber. It has been discussed the nature of the instability in terms of the structural sensitivity and later by the complex-valued endogeneity map. It has been argued that the guided jet wave is responsible for the closure of the feedback mechanism initiated by the shear layer instability. The guided jet mode is the consequence of the intense production of divergence of the velocity perturbations at an axial distance around a diameter from the wall, which has been identified using a novel decomposed structural sensitivity, suited to identify these type of non-local acoustic-hydrodynamic feedbacks. Such an instability mechanism is responsible for the strong emission of tonal noise. First it is robust, the mechanism is weakly sensitive to external perturbations, which could be due to inflow perturbations or the interaction with vortices issued from the region near the wall and initiated by the roll-up of the radial vortex sheet. Second, the emission

of sound is strong, a feature that is observed when considering the relative amplitude between vortical and acoustic pressure of the linear mode. So, in this sense, linear stability is relevant to determine the possibility of strong sound emissions. On the other hand, at low Mach numbers, the main source of sound comes from *vortex-sound*. The structural sensitivity peaks along the radial vortex-sheet, which is the region with the largest module of the linearised Lamb vector. The difference in the mechanisms have several consequences in the non-linear dynamics. The dynamics of the vorticity field in a region around the radial vortex-sheet becomes rapidly chaotic with small variations of the Reynolds number from the primary Hopf bifurcation. Physically, the low temporal coherence of the vortical sources of sound, which are responsible for the emission of the pressure wave closing the feedback-loop, are at the origin of the measured broadband spectrum of the acoustic pressure field. We provide a reduced model, issued from a weakly non-linear analysis, to account for the qualitative changes in dynamics between low and large subsonic Mach numbers. The deterministic model mimics some features of the actual dynamics, such as the frequency-locking of a third tone with the other two or the appearance of a third slow frequency. Nevertheless, due to the truncation to third order, the model does not display chaotic dynamics. Based on a phenomenological reasoning, we propose a stochastic model which accounts for the low temporal coherence of the sources of sound at low Mach number, which in turn induce a frequency mismatch ($\delta\omega$). Such a model is able to reasonably reproduce the sound pressure level spectrums measured from time-stepping simulations. There exist several appealing perspectives. To mention some, it might be of interest to determine from experimental turbulent rounded impinging jets the coefficients of the normal form with data-assimilation techniques, cf Cenedese *et al.* (2022). In addition, the non-local structural sensitivity map may help to investigate the fine details of the instability mechanism in many other configurations where the instability is issued of a non-local feedback, such as airfoil noise, screech, or cavity flows.

Appendix A. Entropy formulation – Decomposition of the adjoint

In this section, we detail the derivation of the decomposition of the adjoint variable $\hat{\mathbf{q}}^\dagger$ into acoustic, vortical and entropic components. Before, proceeding to the detailed description of the adjoint equations, we introduce the linearised compressible Navier–Stokes equations in the primitive variables $[\hat{\rho}, \hat{\mathbf{u}}, \hat{s}, \hat{T}, \hat{p}]^T$. The motivation to introduce this set of equations is because they have a simpler decomposition. The linearised equations are

$$\left(-i\omega \mathbf{B}|_{\mathbf{q}_0} + \mathbf{D}\mathbf{F}|_{\mathbf{q}_0} \right) \hat{\mathbf{q}} = 0, \text{ with } \mathbf{B}|_{\mathbf{q}_0} = \text{diag}(1, \rho_0 \mathbf{I}, \rho_0 T_0, 0, 0), \quad (\text{A } 1)$$

$$\mathbf{D}\mathbf{F}|_{\mathbf{q}_0} \hat{\mathbf{q}} = \begin{cases} \mathbf{u}_0 \cdot \nabla \hat{\rho} + \hat{\rho} \nabla \cdot \mathbf{u}_0 + \hat{\mathbf{u}} \cdot \nabla \rho_0 + \rho_0 \nabla \cdot \hat{\mathbf{u}} & (\text{A } 2a) \\ \hat{\rho} \mathbf{u}_0 \cdot \nabla \mathbf{u}_0 + \rho_0 \mathbf{u}_0 \cdot \nabla \hat{\mathbf{u}} + \rho_0 \hat{\mathbf{u}} \cdot \nabla \mathbf{u}_0 + \nabla \hat{p} - \frac{1}{\text{Re}} \nabla \cdot \tau(\hat{\mathbf{u}}) & (\text{A } 2b) \\ -\gamma(\gamma-1) \frac{M_\infty^2}{\text{Re}} (\tau(\hat{\mathbf{u}}) : \mathbf{D}(\mathbf{u}_0) + \tau(\mathbf{u}_0) : \mathbf{D}(\hat{\mathbf{u}})) - \frac{\gamma}{\text{Pr Re}} \Delta \hat{T} \\ + \rho_0 T_0 \mathbf{u}_0 \cdot \nabla \hat{s} + \rho_0 T_0 \hat{\mathbf{u}} \cdot \nabla s_0 + \hat{\rho} T_0 \mathbf{u}_0 \cdot \nabla s_0 + \rho_0 \hat{T} \mathbf{u}_0 \cdot \nabla s_0 & (\text{A } 2c) \\ \rho_0 T_0 \hat{s} + (\gamma-1) T_0 \hat{\rho} - \rho_0 \hat{T} & (\text{A } 2d) \\ - \rho_0 \hat{T} - \hat{\rho} T_0 + \gamma M_\infty^2 \hat{p} & (\text{A } 2e) \end{cases}$$

And their adjoint counterpart are

$$\left(i\bar{\omega}\mathbf{B}|_{\mathbf{q}_0} + \mathbf{DF}^\dagger|_{\mathbf{q}_0} \right) \hat{\mathbf{q}}^\dagger = 0, \text{ with } \mathbf{B}|_{\mathbf{q}_0} = \text{diag}(1, \rho_0 \mathbf{I}, \rho_0 T_0, 0, 0), \quad (\text{A } 3)$$

$$\mathbf{DF}^\dagger|_{\mathbf{q}_0} \hat{\mathbf{q}}^\dagger = \begin{cases} -\mathbf{u}_0 \cdot \nabla \hat{\rho}^\dagger + (\mathbf{u}_0 \cdot \nabla \mathbf{u}_0) \cdot \hat{\mathbf{u}}^\dagger \\ + (\mathbf{u}_0 \cdot \nabla s_0) \hat{s}^\dagger + T_0((\gamma - 1) \hat{T}^\dagger - \hat{p}^\dagger) \\ - \rho_0 \mathbf{u}_0 \cdot \nabla \hat{\mathbf{u}}^\dagger + \rho_0 \hat{\mathbf{u}}^\dagger \cdot (\nabla \mathbf{u}_0)^T - \frac{1}{\text{Re}} \nabla \cdot \tau(\hat{\mathbf{u}}^\dagger) \\ - \rho_0 \nabla \hat{\rho}^\dagger + 2\gamma(\gamma - 1) \frac{M_\infty^2}{\text{Re}} \nabla \cdot (\hat{s}^\dagger \tau(\mathbf{u}_0)) + \rho_0 T_0 \hat{s}^\dagger \nabla s_0 \\ - \rho_0 T_0 \mathbf{u}_0 \cdot \nabla \hat{s}^\dagger + \rho_0 T_0 \hat{T}^\dagger \\ \rho_0 T_0 \hat{s}^\dagger \mathbf{u}_0 \cdot \nabla s_0 - \frac{\gamma}{\text{Pr Re}} \nabla^2 \hat{s}^\dagger - \rho_0 \hat{p}^\dagger - \rho_0 \hat{T}^\dagger \\ \gamma M_\infty^2 \hat{p}^\dagger - \nabla \cdot \hat{\mathbf{u}}^\dagger \end{cases} \quad \begin{array}{l} (\text{A } 4a) \\ (\text{A } 4b) \\ (\text{A } 4c) \\ (\text{A } 4d) \\ (\text{A } 4e) \end{array}$$

A.1. Decomposition of the global mode

We first detail how we decompose the global mode $\hat{\mathbf{q}}$ into: *acoustic*, *hydrodynamic* and *entropic* components.

We adopt a Helmholtz-Hodge decomposition (Schoder *et al.* 2020) of the perturbation velocity field into *acoustic* (potential) and *hydrodynamic* (solenoidal)

$$\hat{\mathbf{u}} = \hat{\mathbf{u}}_{\text{ac}} + \hat{\mathbf{u}}_{\text{hyd}} = \nabla \phi_c + \nabla \times \Psi \quad (\text{A } 5)$$

applying divergence to eq. (4.1), the potential ϕ_c is determined from the following Poisson equation

$$\begin{aligned} \Delta \phi_c &= \nabla \cdot \hat{\mathbf{u}} && \text{in } \Omega \\ \nabla \phi_c \cdot \mathbf{n} &= \hat{\mathbf{u}} \cdot \mathbf{n} && \text{on } \partial\Omega. \end{aligned} \quad (\text{A } 6)$$

The hydrodynamic component of the velocity is subsequently determined by subtracting $\hat{\mathbf{u}}_{\text{hyd}} = \hat{\mathbf{u}} - \hat{\mathbf{u}}_{\text{ac}} = \hat{\mathbf{u}} - \nabla \phi_c$. Note that, the uniqueness of the Helmholtz decomposition is subjected to the L^2 -orthogonality condition, in our case satisfied by the suitable boundary condition of eq. (A 6), and the decay of the velocity field at the far-field (Schoder *et al.* 2020).

The pressure decomposition is derived from the linearised momentum equation. Considering an isentropic relationship between density and pressure fluctuations, i.e., $\hat{\rho} T_0 = M_\infty^2 \hat{p}$, and taking divergence of the linearised momentum equation, we end up with the following elliptic equation for the pressure,

$$\begin{aligned} -\frac{1}{\rho_0} \Delta \hat{p} + \frac{\nabla \rho_0 \cdot \nabla \hat{p}}{\rho_0^2} - \nabla \cdot \left(\frac{M_\infty^2}{T_0} (\mathbf{u}_0 \cdot \nabla \mathbf{u}_0) \frac{\hat{p}}{\rho_0} \right) &= \nabla \cdot (\mathbf{u}_0 \cdot \nabla \hat{\mathbf{u}}) + \nabla \cdot (\hat{\mathbf{u}} \cdot \nabla \mathbf{u}_0) \\ &\quad + i\omega \nabla \cdot \hat{\mathbf{u}} - \frac{1}{\text{Re}} \nabla \cdot (\nabla \cdot \tau(\hat{\mathbf{u}})). \end{aligned} \quad (\text{A } 7)$$

Decomposing the velocity field into acoustic and hydrodynamic and leaving the viscous dissipation term to the entropic component, we end up with the following decomposition

of the pressure,

$$-\frac{1}{\rho_0} \Delta \hat{p}_{\text{ac}} + \frac{\nabla \rho_0 \cdot \nabla \hat{p}_{\text{ac}}}{\rho_0^2} - \nabla \cdot \left(\frac{M_\infty^2}{T_0} (\mathbf{u}_0 \cdot \nabla \mathbf{u}_0) \frac{\hat{p}_{\text{ac}}}{\rho_0} \right) = i\omega \nabla \cdot \hat{\mathbf{u}}_{\text{ac}} + \nabla \cdot (\mathbf{u}_0 \cdot \nabla \hat{\mathbf{u}}_{\text{ac}}) + \nabla \cdot (\hat{\mathbf{u}}_{\text{ac}} \cdot \nabla \mathbf{u}_0) \quad (\text{A } 8a)$$

$$-\frac{1}{\rho_0} \Delta \hat{p}_{\text{hyd}} + \frac{\nabla \rho_0 \cdot \nabla \hat{p}_{\text{hyd}}}{\rho_0^2} - \nabla \cdot \left(\frac{M_\infty^2}{T_0} (\mathbf{u}_0 \cdot \nabla \mathbf{u}_0) \frac{\hat{p}_{\text{hyd}}}{\rho_0} \right) = \nabla \cdot (\mathbf{u}_0 \cdot \nabla \hat{\mathbf{u}}_{\text{hyd}}) + \nabla \cdot (\hat{\mathbf{u}}_{\text{hyd}} \cdot \nabla \mathbf{u}_0) \quad (\text{A } 8b)$$

$$\hat{p}_s = \hat{p} - \hat{p}_{\text{hyd}} - \hat{p}_{\text{ac}}. \quad (\text{A } 8c)$$

A.2. Decomposition of the adjoint mode

Before introducing the decomposition of the adjoint global mode, we first review the significance of the decomposition in a simpler example, where we only consider the momentum equation. We introduce a harmonic forcing \mathbf{H}_u to the momentum equation,

$$-i\omega \rho_0 \hat{\mathbf{u}} + \hat{\rho} \mathbf{u}_0 \cdot \nabla \mathbf{u}_0 + \rho_0 \mathbf{u}_0 \cdot \nabla \hat{\mathbf{u}} + \rho_0 \mathbf{u}_0 \cdot \nabla \hat{\mathbf{u}} - \nabla \hat{p} + \frac{1}{\text{Re}} \nabla \cdot \tau(\hat{\mathbf{u}}) = \rho_0 \mathbf{H}_u. \quad (\text{A } 9)$$

The introduction of the forcing term \mathbf{H}_u induces a response of the velocity field $\hat{\mathbf{u}}$ and the pressure field \hat{p} . In the presence of viscous dissipation, the introduction of the momentum source term always excites an entropic response. However, such a component is expected to become of lesser importance at larger Reynolds numbers and to be localized near wall boundaries and in regions of large magnitudes of the shear tensor. For such a reason, we propose the decomposition of the velocity adjoint into hydrodynamical and acoustic components, but having in mind that this is not a perfect decomposition since they should possess a possibly small entropic part. The excitation of the dilation of velocity is evaluated by taking the divergence of the linearised momentum equation eq. (A 9),

$$\begin{aligned} -i\omega \nabla \cdot \hat{\mathbf{u}} &+ \frac{\hat{\rho}}{\rho_0} \nabla \cdot \nabla (\mathbf{u}_0 \mathbf{u}_0) + \nabla \left(\frac{\hat{\rho}}{\rho_0} \right) \cdot \nabla (\mathbf{u}_0 \mathbf{u}_0) \\ &+ \nabla \cdot \nabla (\mathbf{u}_0 \hat{\mathbf{u}}) - \Delta \left(\frac{\hat{p}}{\rho_0} \right) + \frac{1}{\text{Re}} \nabla \cdot (\nabla \cdot \tau(\hat{\mathbf{u}})) = \nabla \cdot \mathbf{H}_u. \end{aligned} \quad (\text{A } 10)$$

Equation (A 10) implies that divergence free forcing terms, i.e., $\nabla \cdot \mathbf{H}_u = 0$, do not excite the acoustic component of the global mode. Furthermore, neglecting viscous dissipation effects, this type of forcing term only excites the hydrodynamic component of the global mode. A similar reasoning leads to the conclusion that, when we neglect viscous dissipation effects, a rotational-free forcing, i.e., $\nabla \times \mathbf{H}_u = 0$, only excites the acoustic component of the perturbation.

Now, interpreting the adjoint global mode as the projector onto the corresponding component of the global mode, we propose a Helmholtz-Hodge decomposition of the adjoint velocity field,

$$\begin{aligned} \hat{\mathbf{u}}^\dagger &= \hat{\mathbf{u}}_{\text{hyd}}^\dagger + \hat{\mathbf{u}}_{\text{ac}}^\dagger = \nabla \phi_c^\dagger + \nabla \times \Psi^\dagger, \\ \Delta \phi_c^\dagger &= \nabla \cdot \hat{\mathbf{u}}^\dagger \text{ in } \Omega \\ \nabla \phi_c^\dagger \cdot \mathbf{n} &= \hat{\mathbf{u}}^\dagger \cdot \mathbf{n} \text{ on } \partial \Omega. \end{aligned} \quad (\text{A } 11)$$

This decomposition is bi-orthogonal when considering only direct and adjoint velocity fields, that is, $\langle \hat{\mathbf{u}}_{\text{hyd}}^\dagger, \rho_0 \hat{\mathbf{u}}_{\text{ac}} \rangle = \langle \hat{\mathbf{u}}_{\text{ac}}^\dagger, \rho_0 \hat{\mathbf{u}}_{\text{hyd}} \rangle = 0$ with $\langle \hat{\mathbf{u}}_{\text{ac}}^\dagger, \rho_0 \hat{\mathbf{u}}_{\text{ac}} \rangle \neq 0$ and $\langle \hat{\mathbf{u}}_{\text{hyd}}^\dagger, \rho_0 \hat{\mathbf{u}}_{\text{hyd}} \rangle \neq 0$. Therefore, the momentum forcing can be expanded as

$$\rho_0 \mathbf{H}_u = \langle \hat{\mathbf{u}}_{\text{hyd}}^\dagger, \rho_0 \mathbf{H}_u \rangle \hat{\mathbf{u}}_{\text{hyd}} + \langle \hat{\mathbf{u}}_{\text{ac}}^\dagger, \rho_0 \mathbf{H}_u \rangle \hat{\mathbf{u}}_{\text{ac}} = \rho_0 \mathbf{H}_{\text{hyd}, u} + \rho_0 \mathbf{H}_{\text{ac}, u}. \quad (\text{A } 12)$$

The next step in the decomposition consists in the decomposition of the entropy adjoint \hat{s}^\dagger . Here below, we justify that $\hat{s}^\dagger = \hat{s}_s^\dagger$, that is, that a forcing term to the entropy equation only excites the entropy component of the global mode. It derives from the fact that we have defined the acoustic and hydrodynamic components to be entropy-free. Evidently, since $\hat{s}_{\text{hyd}}^\dagger = \hat{s}_{\text{ac}}^\dagger = 0$, the decomposition is bi-orthogonal in the entropy variable.

From these considerations, we can derive the remaining components of adjoint. Substituting the gradient of the density adjoint $\nabla \hat{\rho}^\dagger$ from eq. (A 4a) into eq. (A 4b) we derive an explicit equation for $\hat{\rho}^\dagger$

$$\begin{aligned} -i\bar{\omega}\hat{\rho}^\dagger = & -i\bar{\omega}\mathbf{u}_0 \cdot \hat{\mathbf{u}}^\dagger - \mathbf{u}_0 \cdot (\mathbf{u}_0 \cdot \nabla \hat{\mathbf{u}}^\dagger) + \mathbf{u}_0 \cdot (\hat{\mathbf{u}}^\dagger \cdot (\nabla \mathbf{u}_0)^T) - \hat{\mathbf{u}}^\dagger \cdot (\mathbf{u}_0 \cdot \nabla \mathbf{u}_0) \\ & + \frac{1}{\text{Re}} \mathbf{u}_0 \cdot \nabla \cdot \tau \hat{\mathbf{u}}^\dagger - 2\gamma(\gamma-1) \frac{M_\infty^2}{\text{Re}} \frac{1}{\rho_0} \mathbf{u}_0 \cdot \nabla \cdot \hat{s}^\dagger \tau(\mathbf{u}_0) \\ & - T_0 \hat{s}^\dagger \mathbf{u}_0 \cdot \nabla s_0 + (\gamma-1) T_0 \hat{T}^\dagger - T_0 \hat{\rho}^\dagger \end{aligned} \quad (\text{A } 13)$$

Substituting $\hat{s}^\dagger = 0$, $\hat{\mathbf{u}}^\dagger = \hat{\mathbf{u}}_{\text{ac}}^\dagger$ (or $\hat{\mathbf{u}}^\dagger = \hat{\mathbf{u}}_{\text{hyd}}^\dagger$), and $\hat{T}^\dagger = -\hat{\rho}^\dagger$, a relationship that is obtained from eq. (A 4) by considering $\hat{s}^\dagger = 0$, we are led to the following decomposition of $\hat{\rho}^\dagger$

$$\begin{aligned} -i\bar{\omega}\hat{\rho}_{\text{ac}}^\dagger = & -i\bar{\omega}\mathbf{u}_0 \cdot \hat{\mathbf{u}}_{\text{ac}}^\dagger - \mathbf{u}_0 \cdot (\mathbf{u}_0 \cdot \nabla \hat{\mathbf{u}}_{\text{ac}}^\dagger) + \mathbf{u}_0 \cdot (\hat{\mathbf{u}}_{\text{ac}}^\dagger \cdot (\nabla \mathbf{u}_0)^T) \\ & - \hat{\mathbf{u}}_{\text{ac}}^\dagger \cdot (\mathbf{u}_0 \cdot \nabla \mathbf{u}_0) - \gamma T_0 \hat{\rho}^\dagger \\ -i\bar{\omega}\hat{\rho}_{\text{hyd}}^\dagger = & -i\bar{\omega}\mathbf{u}_0 \cdot \hat{\mathbf{u}}_{\text{hyd}}^\dagger - \mathbf{u}_0 \cdot (\mathbf{u}_0 \cdot \nabla \hat{\mathbf{u}}_{\text{hyd}}^\dagger) + \mathbf{u}_0 \cdot (\hat{\mathbf{u}}_{\text{hyd}}^\dagger \cdot (\nabla \mathbf{u}_0)^T) \end{aligned} \quad (\text{A } 14)$$

And the entropic component is determined as $\hat{\rho}_s^\dagger = \hat{\rho}^\dagger - \hat{\rho}_{\text{ac}}^\dagger - \hat{\rho}_{\text{hyd}}^\dagger$. The decomposition of $\hat{\rho}^\dagger$ is not generally bi-orthogonal with respect to the density decomposition of the global mode.

Overall, the adjoint is decomposed as follows,

$$\begin{aligned} \hat{\mathbf{u}}^\dagger &= \hat{\mathbf{u}}_{\text{hyd}}^\dagger + \hat{\mathbf{u}}_{\text{ac}}^\dagger = \nabla \phi_c^\dagger + \nabla \times \Psi^\dagger, \text{ from eq. (A 11)} \\ \hat{s}^\dagger &= \hat{s}_s^\dagger \\ \hat{\rho}^\dagger &= \hat{\rho}_{\text{ac}}^\dagger + \hat{\rho}_{\text{hyd}}^\dagger + \hat{\rho}_s^\dagger \\ \hat{\rho}^\dagger &= \hat{\rho}_{\text{ac}}^\dagger = \frac{\nabla \cdot \hat{\mathbf{u}}^\dagger}{\gamma M_\infty^2} \\ \hat{T}^\dagger &= \hat{T}_{\text{ac}}^\dagger + \hat{T}_s^\dagger = -\frac{\nabla \cdot \hat{\mathbf{u}}^\dagger}{\gamma M_\infty^2} + (\hat{s}^\dagger \mathbf{u}_0 \cdot \nabla s_0 - \frac{\gamma}{\text{Pr Re}} \frac{1}{\rho_0} \Delta s_0) \end{aligned} \quad (\text{A } 15)$$

Appendix B. Normal form reduction

Here, we discuss the computation of the coefficients of the normal form eq. (B 20). These are computed following a multiple scales expansion of the solution \mathbf{q} of eq. (2.1). We rewrite the governing equations as follows,

$$\mathbf{B} \frac{\partial \mathbf{q}}{\partial t} = \mathbf{F}(\mathbf{q}, \boldsymbol{\eta}) \equiv -\left(\mathbf{c} + \mathbf{L}\mathbf{q} + \frac{1}{2} \mathbf{N}_2(\mathbf{q}, \mathbf{q}) + \frac{1}{6} \mathbf{N}_3(\mathbf{q}, \mathbf{q}, \mathbf{q}) + \mathbf{G}_1(\mathbf{q}, \boldsymbol{\eta}) + \frac{1}{2} \mathbf{G}_2(\mathbf{q}, \mathbf{q}, \boldsymbol{\eta}) \right), \quad (\text{B } 1)$$

where $\mathbf{c} = [0, \mathbf{0}, 0, 1]^T$, \mathbf{B} is the mass matrix, \mathbf{L} the linear operator on the state variable \mathbf{q} , and \mathbf{G}_1 and \mathbf{G}_2 the linear and quadratic operators in the state variable \mathbf{q} and parameters $\boldsymbol{\eta}$. These operators are defined as

$$\mathbf{B} = \begin{pmatrix} 1 & 0 & 0 & 0 \\ 0 & \rho\mathbf{I} & 0 & 0 \\ 0 & 0 & \rho & 0 \\ 0 & 0 & 0 & 0 \end{pmatrix}, \quad \mathbf{L} = \begin{pmatrix} 0 & 0 & 0 & 0 \\ 0 & 0 & 0 & \nabla \\ 0 & 0 & 0 & 0 \\ 0 & 0 & 0 & 0 \end{pmatrix},$$

$$\mathbf{G}_1(\mathbf{q}, \boldsymbol{\eta}) = \begin{pmatrix} 0 & 0 & 0 & 0 \\ 0 & -\frac{1}{Re}\nabla \cdot \tau(\cdot) & 0 & 0 \\ 0 & 0 & -\frac{\gamma}{Pr Re}\Delta & 0 \\ 0 & 0 & 0 & \gamma M_\infty^2 \end{pmatrix}, \quad (\text{B } 2)$$

$$\mathbf{G}_2(\mathbf{q}_1, \mathbf{q}_1, \boldsymbol{\eta}) = \begin{pmatrix} 0 \\ \mathbf{0} \\ -(\gamma - 1)\gamma M_\infty^2 / Re(\tau(\mathbf{u}_1) : \mathbf{D}(\mathbf{u}_2) + \tau(\mathbf{u}_2) : \mathbf{D}(\mathbf{u}_1)) \\ 0 \end{pmatrix},$$

while the quadratic nonlinear operator on the state variable is defined as

$$\mathbf{N}_2(\mathbf{q}_1, \mathbf{q}_2) = \begin{pmatrix} \mathbf{u}_1 \cdot \nabla \rho_2 + \mathbf{u}_2 \cdot \nabla \rho_1 + \rho_1 \nabla \cdot \mathbf{u}_2 + \rho_2 \nabla \cdot \mathbf{u}_1 \\ 0 \\ 0 \\ -(\rho_1 T_2 + \rho_2 T_1) \end{pmatrix}, \quad (\text{B } 3)$$

and cubic nonlinear operator on the state variable is

$$\mathbf{N}_3(\mathbf{q}_1, \mathbf{q}_2, \mathbf{q}_3) = \begin{pmatrix} 0 \\ \sum_{i,j,k} \rho_i \mathbf{u}_j \cdot \nabla \mathbf{u}_k \\ \sum_{i,j,k} (\gamma - 1) \rho_i T_j \nabla \cdot \mathbf{u}_k + \rho_i \mathbf{u}_j \cdot \nabla T_k \\ 0 \end{pmatrix}, \quad (\text{B } 4)$$

The expansion considers a two scale development of the original time $t \mapsto t + \varepsilon^2 \tau$, here ε is the order of magnitude of the flow disturbances, assumed small $\varepsilon \ll 1$. Herein, we consider the small parameters ε_{M^2} and ε_ν , which are a function of the Mach number and Reynolds numbers at the far-field,

$$\varepsilon_{M^2}^2 = (M_{\infty,c}^2 - M_\infty^2) \sim \varepsilon^2 \text{ and } \varepsilon_\nu^2 = (\nu_c - \nu) = (Re_c^{-1} - Re^{-1}) \sim \varepsilon^2.$$

With this compact notation we can provide an explicit form of the linearized Navier–Stokes equations with respect to baseflow \mathbf{q}_b ,

$$\mathbf{DF}|_{\mathbf{q}_b}(\mathbf{q}, \boldsymbol{\eta}) \equiv \mathbf{L}\mathbf{q} + \mathbf{N}_2(\mathbf{q}_b, \mathbf{q}) + \frac{1}{2}\mathbf{N}_3(\mathbf{q}_b, \mathbf{q}_b, \mathbf{q}) + \mathbf{G}_1(\mathbf{q}, \boldsymbol{\eta}) + \mathbf{G}_2(\mathbf{q}_b, \mathbf{q}, \boldsymbol{\eta}). \quad (\text{B } 5)$$

The technique decomposes time into a fast timescale t of the phase associated to the self-sustained instabilities and a slow timescale related to the evolution of the amplitudes $z_i(\tau)$, introduced in eq. (2.11), for $i = 1, 2, 3$. The ansatz of the expansion is as follows

$$\mathbf{q}(t, \tau) = \mathbf{q}_b + \varepsilon \mathbf{q}_{(\varepsilon)}(t, \tau) + \varepsilon^2 \mathbf{q}_{(\varepsilon^2)}(t, \tau) + \varepsilon^3 \mathbf{q}_{(\varepsilon^3)}(t, \tau) + O(\varepsilon^4) \quad (\text{B } 6)$$

In such a case, the vector is expanded as

$$\mathbf{q}_{(\varepsilon)}(t, \tau) = \sum_{k=1}^N (z_k(\tau) \hat{\mathbf{q}}_{(z_k)}(r, z) e^{i\omega_k t} + \text{c.c.}) \quad (\text{B } 7)$$

Note that the expansion of the LHS of eq. (2.1) up to third order is as follows

$$\varepsilon \mathbf{B} \frac{\partial \mathbf{q}(\varepsilon)}{\partial t} + \varepsilon^2 \mathbf{B} \frac{\partial \mathbf{q}(\varepsilon^2)}{\partial t} + \varepsilon^3 [\mathbf{B} \frac{\partial \mathbf{q}(\varepsilon^3)}{\partial t} + \mathbf{B} \frac{\partial \mathbf{q}(\varepsilon)}{\partial \tau}] + O(\varepsilon^4), \quad (\text{B } 8)$$

and the RHS respectively,

$$\mathbf{F}(\mathbf{q}, \boldsymbol{\eta}) = \mathbf{F}_{(0)} + \varepsilon \mathbf{F}_{(\varepsilon)} + \varepsilon^2 \mathbf{F}_{(\varepsilon^2)} + \varepsilon^3 \mathbf{F}_{(\varepsilon^3)} + O(\varepsilon^4). \quad (\text{B } 9)$$

In the following, in order to improve readability, we define the set of vectors of linear, quadratic, and secular interactions.

$$\begin{aligned} \mathbf{Z} &\equiv \{z_1, z_2, z_3\}, \quad \bar{\mathbf{Z}} = \{\bar{z}_1, \bar{z}_2, \bar{z}_3\} \\ \mathbf{Z}^2 &\equiv \mathbf{Z} \otimes \mathbf{Z} \oplus \mathbf{Z} \otimes \bar{\mathbf{Z}} = \{z_1^2, z_2^2, z_3^2, z_1 z_2, z_1 z_3, z_2 z_3, |z_1|^2, |z_2|^2, |z_3|^2, \\ &\quad z_1 \bar{z}_2, z_1 \bar{z}_3, z_2 \bar{z}_3\} \\ \mathbf{Z}_S &\equiv \{z_1, z_2, z_3, z_1 |z_1|^2, z_1 |z_2|^2, z_1 |z_3|^2, z_2 |z_1|^2, z_2 |z_2|^2, z_2 |z_3|^2, \\ &\quad z_3 |z_1|^2, z_3 |z_2|^2, z_3 |z_3|^2, z_1 \bar{z}_2 z_3, z_2 \bar{z}_3, z_2 \bar{z}_1\} \end{aligned} \quad (\text{B } 10)$$

where only unique elements are kept. We denote by \mathbf{z}_α^n any element of the family \mathbf{Z}^n , with $n \in \mathbb{N}^*$.

B.1. Zeroth order

The zeroth order corresponds to the steady-state problem of the governing equations evaluated at the parameter vector $\boldsymbol{\eta} = (M_\infty, Re)^T$,

$$\mathbf{0} = \mathbf{F}(\mathbf{q}_b, \boldsymbol{\eta}) \quad (\text{B } 11)$$

whose solution is the steady state \mathbf{q}_b .

B.2. First order

The first order corresponds to the resolution of a homogeneous linear system, i.e., a generalized eigenvalue problem evaluated. The eigenpairs $[i\omega_\ell, \hat{\mathbf{q}}_{(z_\ell)}]$ are determined as the solutions of the following *shifted* (Meliga *et al.* 2009) eigenvalue problem

$$\tilde{\mathbf{J}}_{\omega_\ell} \hat{\mathbf{q}}_{(z_\ell)} = \left(i\omega_\ell \mathbf{B} - \varepsilon^2 \mathbf{S} - \mathbf{D}\mathbf{F}|_{\mathbf{q}_b}(\mathbf{q}, \boldsymbol{\eta}) \right) \hat{\mathbf{q}}_{(z_\ell)} \quad (\text{B } 12)$$

where we have introduced the shift operator $\varepsilon^2 \mathbf{S}$, which is defined in such a way that $\tilde{\mathbf{J}}_{\omega_\ell} \hat{\mathbf{q}}_{(z_\ell)} = \mathbf{0}$ at $\boldsymbol{\eta}$ and $\text{Im}(\omega_\ell) = 0$, and $\mathbf{S}\mathbf{q} = \mathbf{0}$ for any other vector field \mathbf{q} distinct to the eigenmodes. The \mathbf{B} -norm of the eigenmodes $\hat{\mathbf{q}}_{(z_\ell)}(r, z)$ is scaled to unity, i.e., $\langle \hat{\mathbf{q}}, \hat{\mathbf{q}} \rangle_{\mathbf{B}} = 1$.

Analogously, the adjoint eigenmodes are determined from the resolution of eq. (2.7) and normalised with respect to the direct mode so the inner product is equal to the unity, i.e., $\langle \hat{\mathbf{q}}^\dagger, \hat{\mathbf{q}} \rangle_{\mathbf{B}} = 1$

B.3. Second order

The second order expansion term $\mathbf{q}_{(\varepsilon^2)}(t, \tau)$ is determined by the resolution of a set of linear systems, where the forcing terms are evaluated from first and zeroth order terms. The expansion in terms of amplitudes $z_\ell(\tau)$ of $\mathbf{q}_{(\varepsilon^2)}(t, \tau)$ is assessed by collecting the

second order forcing terms. Non-linear second order terms in ε are

$$\begin{aligned} \mathbf{F}_{(\varepsilon^2)} &\equiv \sum_{j,k=1}^3 \frac{1}{2} \left(z_j z_k \mathbf{N}_2(\hat{\mathbf{q}}_{(z_j)}, \hat{\mathbf{q}}_{(z_k)}) e^{-i(\omega_j + \omega_k)t} + \text{c.c.} \right) \\ &+ \sum_{j,k=1}^3 \frac{1}{2} \left(z_j \bar{z}_k \mathbf{N}_2(\hat{\mathbf{q}}_{(z_j)}, \hat{\mathbf{q}}_{(\bar{z}_k)}) e^{-i(\omega_j - \omega_k)t} + \text{c.c.} \right) \\ &+ \sum_{\ell=1}^2 \eta_\ell \mathbf{G}_1(\mathbf{q}_b, \mathbf{e}_\ell), \end{aligned} \quad (\text{B } 13)$$

where \mathbf{e}_ℓ is an element of the orthonormal basis of \mathbb{R}^2 . Then the second order expansion of the flow variable is carried out, so it matches the terms of the forcing

$$\mathbf{q}_{(\varepsilon^2)} \equiv \sum_{\mathbf{z}_\alpha^2 \in \mathbf{Z}^2} \left(\mathbf{z}_\alpha^2 \hat{\mathbf{q}}_{(\mathbf{z}_\alpha^2)} e^{-i\omega_\alpha t} + \text{c.c.} \right) + \sum_{\ell=1}^2 \eta_\ell \mathbf{q}_b^{(\eta_\ell)}, \quad (\text{B } 14)$$

The terms $\hat{\mathbf{q}}_{(z_j^2)}$ are harmonics of the flow, $\hat{\mathbf{q}}_{(z_j z_k)}$ with $j \neq k$ are coupling terms, $\hat{\mathbf{q}}_{(|z_j|^2)}$ are harmonic base flow modification terms and $\mathbf{q}_b^{(\eta_\ell)}$ are base flow corrections due to a modification of the parameter η_ℓ from the critical point. Then the second order terms are determined from the resolution of the following (non-singular) systems of equations

$$\mathbf{J}_{(\omega_j + \omega_k)} \hat{\mathbf{q}}_{(z_j z_k)} = \hat{\mathbf{F}}_{(z_j z_k)}, \quad (\text{B } 15)$$

where $\hat{\mathbf{F}}_{(z_j z_k)}$ is the term of eq. (B 13) proportional to $z_j z_k$ and

$$\mathbf{J}_{(0,0)} \mathbf{Q}_b^{(\eta_\ell)} = \mathbf{G}(\mathbf{Q}_b, \mathbf{e}_\ell). \quad (\text{B } 16)$$

B.4. Third order

At third order, we proceed as for previous orders, first the forcing term is expanded

$$\begin{aligned} \mathbf{F}_{(\varepsilon^3)} &\sum_{\mathbf{z}_\alpha \in \mathbf{Z}, \mathbf{z}_\beta^2 \in \mathbf{Z}^2} \mathbf{z}_\alpha \mathbf{z}_\beta^2 [\mathbf{N}(\hat{\mathbf{q}}_{(\mathbf{z}_\beta^2)}, \hat{\mathbf{q}}_{(\mathbf{z}_\alpha)})] e^{i(\omega_\alpha + \omega_\beta)t} \\ &\sum_{\mathbf{z}_\alpha \in \mathbf{Z}, \mathbf{z}_\beta \in \mathbf{Z}, \mathbf{z}_\gamma \in \mathbf{Z}} \mathbf{z}_\alpha \mathbf{z}_\beta \mathbf{z}_\gamma [\mathbf{N}_3(\hat{\mathbf{q}}_{(\mathbf{z}_\gamma)}, \hat{\mathbf{q}}_{(\mathbf{z}_\beta)}, \hat{\mathbf{q}}_{(\mathbf{z}_\alpha)})] e^{i(\omega_\alpha + \omega_\beta + \omega_\gamma)t} \\ &+ \sum_{j=1}^2 \sum_{\ell=1}^2 \left[z_j \eta_\ell [\mathbf{N}_2(\hat{\mathbf{q}}_{(z_j)}, \mathbf{Q}_b^{(\eta_\ell)})] e^{-i\omega_j t} + \text{c.c.} \right] \\ &+ \sum_{j=1}^2 \sum_{\ell=1}^2 \left[z_j \eta_\ell \mathbf{G}_1(\hat{\mathbf{q}}_{(z_j)}, \mathbf{e}_\ell) e^{-i\omega_j t} + \text{c.c.} \right] + \sum_{j=1}^3 z_j \mathbf{S} \hat{\mathbf{q}}_{(z_j)}, \end{aligned} \quad (\text{B } 17)$$

Followed, by the expansion of the third-order secular terms $\mathbf{q}_{(\varepsilon^3)}(t, \tau)$

$$\begin{aligned} \mathbf{q}_{(\varepsilon^3)}(t, \tau) &\equiv \sum_{\substack{\mathbf{z}_\alpha \in \mathbf{Z}_S \\ 2 \\ 2}} \left[\mathbf{z}_\alpha^3 \hat{\mathbf{q}}_{(\mathbf{z}_\alpha)} e^{-i\omega_\alpha t} + \text{c.c.} \right] \\ &+ \sum_{j=1}^2 \sum_{\ell=1}^2 \left[z_j \eta_\ell \mathbf{Q}_{(z_j)}^{(\eta_\ell)} e^{-i\omega_j t} + \text{c.c.} \right] \end{aligned} \quad (\text{B } 18)$$

To ensure the solvability of the resonant terms we must enforce compatibility conditions, i.e. the *Fredholm alternative*. The resonant terms are then determined from the resolution

ν_{11}	ν_{12}	ν_{13}	ν_{21}	ν_{22}	ν_{23}
$-0.57 - 0.28i$	$-0.04 + 0.13i$	$-1.3 - 1.2i$	$-0.1 - 0.23i$	$-0.25 - 0.94i$	$-0.15 - 2.5i$
ν_{31}	ν_{32}	ν_{33}	χ_1	χ_2	χ_3
$-1.6 + 2.3i$	$-1.0 + 0.48i$	$-0.76 + 0.34i$	$1.7 - 1.8i$	$-0.27 - 0.61i$	$-3.0 - 1.7i$

Table 5: $M_\infty = 0.3$.

ν_{11}	ν_{12}	ν_{13}	ν_{21}	ν_{22}	ν_{23}
$-0.068 + 0.032i$	$-0.025 + 0.028i$	$-0.33 + 0.076i$	$-0.10 + 0.090i$	$-0.27 + 0.23i$	$-0.34 + 0.076i$
ν_{31}	ν_{32}	ν_{33}	χ_1	χ_2	χ_3
$-0.15 + 0.022i$	$-0.43 - 0.009i$	$-0.25 - 0.15i$	$-0.015 - 0.047i$	$-0.076 + 0.033i$	$-0.065 - 0.048i$

Table 6: $M_\infty = 0.5$.

of the following set of *bordered systems*

$$\begin{pmatrix} \mathbf{J}_{(\omega_k, m_k)} & \hat{\mathbf{q}}_{(z_k)} \\ \hat{\mathbf{q}}_{(z_k)}^\dagger & 0 \end{pmatrix} \begin{pmatrix} \hat{\mathbf{q}}_{(\mathbf{z}_\alpha^{(S)})} \\ s \end{pmatrix} = \begin{pmatrix} \hat{\mathbf{F}}_{(\mathbf{z}_\alpha^{(S)})} \\ 0 \end{pmatrix}, \quad \mathbf{z}_\alpha^{(S)} \in \mathbf{Z}_S \quad (\text{B } 19)$$

where $s = \lambda_k^{(\varepsilon_\nu^2)}$ (respectively $s = \lambda_k^{(\varepsilon_{M_\infty^2})}$) for $\mathbf{z}_\alpha^{(S)} = z_k$ and $s = \nu_{kl}^{(0)}$ for $\mathbf{z}_\alpha^{(S)} = z_k |z_\ell|^2$ and $s = \chi_1$ for $\mathbf{z}_\alpha^{(S)} = z_2^2 \bar{z}_3$, $s = \chi_2$ for $\mathbf{z}_\alpha^{(S)} = z_1 \bar{z}_2 z_3$, and $s = \chi_3$ for $\mathbf{z}_\alpha^{(S)} = z_2^2 \bar{z}_1$.

Table 5 and table 6 list the cubic coefficients of the normal form for the two considered Mach numbers based on the far-field speed of sound (M_∞).

B.5. Example of a larger number of mode interactions

The general case with arbitrary N limit cycles may be expressed as

$$\dot{z}_j = z_j (\lambda_j + \sum_{k=1}^N \nu_{jk} |z_k|^2) + \text{NL}_{j,\text{res}} \quad \text{for } j = 1, \dots, N \quad (\text{B } 20)$$

where $\text{NL}_{j,\text{res}}$ are the resonant terms at the third order. For $N = 5$, the resonant term is as follows,

$$\text{NL}_{\text{res}} = \left[\begin{array}{l} \chi_{1,1} z_2^2 \bar{z}_3 + \chi_{1,2} z_2 z_3 \bar{z}_4 + \chi_{1,3} z_2 z_4 \bar{z}_5 + \chi_{1,4} z_3^2 \bar{z}_5 \\ \chi_{2,1} z_1 \bar{z}_2 z_3 + \chi_{2,2} z_1 z_4 \bar{z}_3 \chi_{2,3} z_1 z_5 \bar{z}_4 \chi_{2,4} z_4^2 \bar{z}_4 + \chi_{2,5} z_3 z_4 \bar{z}_5 \\ \chi_{3,1} z_2^2 \bar{z}_1 + \chi_{3,2} z_2 \bar{z}_3 z_4 + \chi_{3,3} z_4^2 \bar{z}_5 \\ \chi_{4,1} z_5 \bar{z}_4 z_3 + \chi_{4,2} z_3^2 \bar{z}_2 + \chi_{4,3} z_3 z_2 \bar{z}_1 \chi_{4,4} z_5 z_2 \bar{z}_3 \chi_{4,5} z_5 z_1 \bar{z}_2 \\ \chi_{5,1} z_4^2 \bar{z}_3 + \chi_{5,2} z_4 z_3 \bar{z}_2 + \chi_{5,3} z_4 z_2 \bar{z}_1 + \chi_{5,4} z_3^2 \bar{z}_1 \end{array} \right] \quad (\text{B } 21)$$

Figure 15 (b) illustrates the resonant interactions for $N = 5$ for the equation of z_3 , i.e. $\text{NL}_{3,\text{res}} = \chi_{3,1} z_2^2 \bar{z}_1 + \chi_{3,2} z_2 \bar{z}_3 z_4 + \chi_{3,3} z_4^2 \bar{z}_5$.

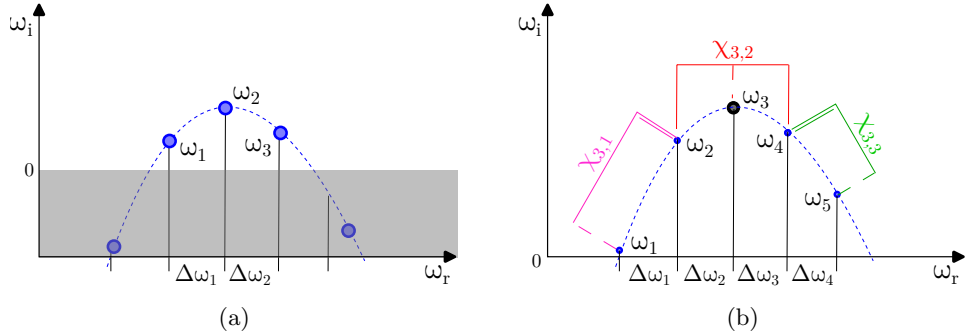


Figure 15: (a) Sketch of the spectrum. (b) Sketch of the spectrum indicating the local contributions to the normal form: (double) solid line indicates the coefficient multiplies the (square) of the mode, dashed line the complex conjugate of the mode.

REFERENCES

- BOGEY, CHRISTOPHE 2021 Acoustic tones in the near-nozzle region of jets: characteristics and variations between mach numbers 0.5 and 2. *Journal of Fluid Mechanics* **921**.

BOGEY, CHRISTOPHE 2022 Tones in the acoustic far field of jets in the upstream direction. *AIAA Journal* **60** (4), 2397–2406.

BOGEY, CHRISTOPHE & GOJON, ROMAIN 2017 Feedback loop and upwind-propagating waves in ideally expanded supersonic impinging round jets. *Journal of Fluid Mechanics* **823**, 562–591.

BRÈS, GUILLAUME A, JORDAN, PETER, JAUNET, VINCENT, LE RALLIC, MAXIME, CAVALIERI, ANDRÉ VG, TOWNE, AARON, LELE, SANJIVA K, COLONIUS, TIM & SCHMIDT, OLIVER T 2018 Importance of the nozzle-exit boundary-layer state in subsonic turbulent jets. *Journal of Fluid Mechanics* **851**, 83–124.

BUCHMANN, NA, MITCHELL, DM, INGVORSEN, KRISTIAN MARK, HONNERY, DR & SORIA, J 2011 High spatial resolution imaging of a supersonic underexpanded jet impinging on a flat plate. In *6th Australian Conference on Laser Diagnostics in Fluid Mechanics and Combustion*.

CALLAHAM, JARED L, LOISEAU, J-C, RIGAS, GEORGIOS & BRUNTON, STEVEN L 2021 Nonlinear stochastic modelling with langevin regression. *Proceedings of the Royal Society A* **477** (2250), 20210092.

CENEDESE, MATTIA, AXÅS, JOAR, BÄUERLEIN, BASTIAN, AVILA, KERSTIN & HALLER, GEORGE 2022 Data-driven modeling and prediction of non-linearizable dynamics via spectral submanifolds. *Nature communications* **13** (1), 872.

CHU, BOA-TEH 1965 On the energy transfer to small disturbances in fluid flow (part i). *Acta Mechanica* **1** (3), 215–234.

DAUPTAIN, A, GICQUEL, LYM & MOREAU, S 2012 Large eddy simulation of supersonic impinging jets. *AIAA journal* **50** (7), 1560–1574.

EDGINGTON-MITCHELL, DANIEL 2019 Aeroacoustic resonance and self-excitation in screeching and impinging supersonic jets—a review. *International Journal of Aeroacoustics* **18** (2-3), 118–188.

EDGINGTON-MITCHELL, DANIEL, JAUNET, VINCENT, JORDAN, PETER, TOWNE, AARON, SORIA, JULIO & HONNERY, DAMON 2018 Upstream-travelling acoustic jet modes as a closure mechanism for screech. *Journal of Fluid Mechanics* **855**, R1.

EWERT, ROLAND & SCHRÖDER, WOLFGANG 2003 Acoustic perturbation equations based on flow decomposition via source filtering. *Journal of Computational Physics* **188** (2), 365–398.

FANI, ANDREA, CITRO, V, GIANNETTI, F & AUTERI, F 2018 Computation of the bluff-body sound generation by a self-consistent mean flow formulation. *Physics of Fluids* **30** (3), 036102.

GIANNETTI, FLAVIO & LUCHINI, PAOLO 2007 Structural sensitivity of the first instability of the cylinder wake. *Journal of Fluid Mechanics* **581**, 167–197.

- GOJON, ROMAIN & BOGEY, CHRISTOPHE 2017a Flow structure oscillations and tone production in underexpanded impinging round jets. *Aiaa Journal* **55** (6), 1792–1805.
- GOJON, ROMAIN & BOGEY, CHRISTOPHE 2017b Numerical study of the flow and the near acoustic fields of an underexpanded round free jet generating two screech tones. *International Journal of Aeroacoustics* **16** (7-8), 603–625.
- GOJON, ROMAIN, BOGEY, CHRISTOPHE & MARSDEN, OLIVIER 2016 Investigation of tone generation in ideally expanded supersonic planar impinging jets using large-eddy simulation. *Journal of Fluid Mechanics* **808**, 90–115.
- HO, CHIH-MING & NOSSEIR, NAGY S 1981 Dynamics of an impinging jet. part 1. the feedback phenomenon. *Journal of Fluid Mechanics* **105**, 119–142.
- HOWE, MS 1975 Contributions to the theory of aerodynamic sound, with application to excess jet noise and the theory of the flute. *Journal of fluid mechanics* **71** (4), 625–673.
- JAUNET, VINCENT, MANCINELLI, MATTEO, JORDAN, PETER, TOWNE, AARON, EDGINGTON-MITCHELL, DANIEL M, LEHNASCH, GUILLAUME & GIRARD, STÈVE 2019 Dynamics of round jet impingement. In *25th AIAA/CEAS Aeroacoustics Conference*, p. 2769.
- JORDAN, PETER, JAUNET, VINCENT, TOWNE, AARON, CAVALIERI, ANDRÉ VG, COLONIUS, TIM, SCHMIDT, OLIVER & AGARWAL, ANURAG 2018 Jet-flap interaction tones. *Journal of Fluid Mechanics* **853**, 333–358.
- MANCINELLI, MATTEO, JAUNET, VINCENT, JORDAN, PETER & TOWNE, AARON 2019 Screech-tone prediction using upstream-travelling jet modes. *Experiments in Fluids* **60** (1), 1–9.
- MARQUES, F, LOPEZ, JM & SHEN, J 2001 A periodically forced flow displaying symmetry breaking via a three-tori gluing bifurcation and two-tori resonances. *Physica D: Nonlinear Phenomena* **156** (1-2), 81–97.
- MARQUET, OLIVIER & LESSHAFT, LUTZ 2015 Identifying the active flow regions that drive linear and nonlinear instabilities. *arXiv preprint arXiv:1508.07620*.
- MELIGA, PHILIPPE, CHOMAZ, JEAN-MARC & SIPP, DENIS 2009 Global mode interaction and pattern selection in the wake of a disk: a weakly nonlinear expansion. *Journal of Fluid Mechanics* **633**, 159–189.
- MELIGA, PHILIPPE, SIPP, D & CHOMAZ, J-M 2010 Effect of compressibility on the global stability of axisymmetric wake flows. *Journal of Fluid Mechanics* **660**, 499–526.
- MITCHELL, DANIEL M, HONNERY, DAMON R & SORIA, JULIO 2012 The visualization of the acoustic feedback loop in impinging underexpanded supersonic jet flows using ultra-high frame rate schlieren. *Journal of visualization* **15** (4), 333–341.
- NEUWERTH, G 1974 Acoustic feedback of a subsonic and supersonic free jet which impinges on an obstacle. *NASA TT F-15719*.
- NEWHOUSE, SHELDON, RUELLE, DAVID & TAKENS, FLORIS 1978 Occurrence of strange axiom a attractors near quasi periodic flows on $t \in \mathbb{R}$, $m \geq 3$. *Communications in Mathematical Physics* **64**, 35–40.
- NORUM, THOMAS D 1991 Supersonic rectangular jet impingement noise experiments. *AIAA journal* **29** (7), 1051–1057.
- NOSSEIR, NAGY S & HO, CHIH-MING 1982 Dynamics of an impinging jet. part 2. the noise generation. *Journal of fluid mechanics* **116**, 379–391.
- POWELL, ALAN 1953 On edge tones and associated phenomena. *Acta Acustica United with Acustica* **3** (4), 233–243.
- POWELL, ALAN 1961 On the edgetone. *The Journal of the Acoustical Society of America* **33** (4), 395–409.
- POWELL, ALAN 1990 Some aspects of aeroacoustics: From rayleigh until today.
- PREISSER, JOHN S 1979 Fluctuating surface pressure and acoustic radiation for subsonic normal jet impingement. *Tech. Rep.*
- RIENSTRA, SJOERD W & HIRSCHBERG, AVRAHAM 2004 An introduction to acoustics. *Eindhoven University of Technology* **18**, 19.
- RISBORG, ADAM & SORIA, JULIO 2009 High-speed optical measurements of an underexpanded supersonic jet impinging on an inclined plate. In *28th international congress on high-speed imaging and photonics*, , vol. 7126, pp. 477–487. SPIE.
- SCHODER, STEFAN, ROPPERT, KLAUS & KALTENBACHER, MANFRED 2020 Helmholtz's decomposition for compressible flows and its application to computational aeroacoustics. *SN Partial Differential Equations and Applications* **1** (6), 1–20.

- SHAABANI-ARDALI, LÉOPOLD, SIPP, DENIS & LESSHAFFT, LUTZ 2019 Vortex pairing in jets as a global floquet instability: modal and transient dynamics. *Journal of Fluid Mechanics* **862**, 951–989.
- SIERRA, JAVIER, FABRE, DAVID & CITRO, VINCENZO 2020a Efficient stability analysis of fluid flows using complex mapping techniques. *Computer Physics Communications* **251**, 107100.
- SIERRA, J, FABRE, DAVID, CITRO, VINCENZO & GIANNETTI, FLAVIO 2020b Bifurcation scenario in the two-dimensional laminar flow past a rotating cylinder. *Journal of Fluid Mechanics* **905**.
- SIERRA-AUSIN, J, FABRE, D, CITRO, V & GIANNETTI, F 2022 Acoustic instability prediction of the flow through a circular aperture in a thick plate via an impedance criterion. *Journal of Fluid Mechanics* **943**, A48.
- SIERRA-AUSÍN, J., LORITE-DÍEZ, M., JIMÉNEZ-GONZÁLEZ, J.I., CITRO, V. & FABRE, D. 2022 Unveiling the competitive role of global modes in the pattern formation of rotating sphere flows. *Journal of Fluid Mechanics* **942**, A54.
- SPIESER, ETIENNE 2020 Modélisation de la propagation du bruit de jet par une méthode adjointe formulée pour l'acoustique potentielle. PhD thesis.
- TAM, CHRISTOPHER KW & AHUJA, KK 1990 Theoretical model of discrete tone generation by impinging jets. *Journal of Fluid Mechanics* **214**, 67–87.
- TAM, CHRISTOPHER KW & CHANDRAMOULI, SATHYANARAYAN 2020 Jet-plate interaction tones relevant to over-the-wing engine mount concept. *Journal of Sound and Vibration* **486**, 115378.
- TANAKA, DAN 2005 Bifurcation scenario to nikolaevskii turbulence in small systems. *Journal of the Physical Society of Japan* **74** (8), 2223–2225.
- TOWNE, AARON, CAVALIERI, ANDRÉ VG, JORDAN, PETER, COLONIUS, TIM, SCHMIDT, OLIVER, JAUNET, VINCENT & BRÈS, GUILLAUME A 2017 Acoustic resonance in the potential core of subsonic jets. *Journal of Fluid Mechanics* **825**, 1113–1152.
- VARÉ, MATHIEU & BOGEY, CHRISTOPHE 2022a Generation of acoustic tones in round jets at a mach number of 0.9 impinging on a plate with and without a hole. *Journal of Fluid Mechanics* **936**.
- VARÉ, MATHIEU & BOGEY, CHRISTOPHE 2022b Mach number dependence of tone generation in impinging round jets. In *28th AIAA/CEAS Aeroacoustics 2022 Conference*, p. 2866.
- WAGNER, FR 1971 *The sound and flow field of an axially symmetric free jet upon impact on a wall*. National Aeronautics and Space Administration.